

Modeling CMAQ dry deposition treatment over Western Pacific: A distinct characteristic of mineral dust and anthropogenic aerosol

Steven Soon-Kai Kong¹, Joshua S. Fu², Neng-Huei Lin^{1,3,*}, Guey-Rong Sheu^{1,3,*}, Wei-Syun Huang¹

¹ Department of Atmospheric Sciences, National Central University, Taoyuan, 32001, Taiwan

² Department of Civil and Environmental Engineering, the University of Tennessee Knoxville, TN37996, USA

³ Center for Environmental Monitoring and Technology, National Central University, Taoyuan, 32001, Taiwan

Correspondence to: Neng-Huei Lin (nhlin@cc.ncu.edu.tw) and Guey-Rong Sheu (grsheu@atm.ncu.edu.tw)

Abstract. Dry deposition plays a vital role in the aerosol removal process from the atmosphere. However, the chemical transport model (CTM) is sensitive to the dry deposition parameterization and yet remains to be determined due to the limited particle deposition measurement. By utilizing the CMAQv5.4 with the refined dust emission treatment, the East Asian dust (EAD) simulation during January 2023 and Spring 2021 was constructed to evaluate the performance of dry deposition parameterizations, namely S22, E20, and P22. The result showed that the dry deposition parameterization could significantly impact the CMAQ dust concentration in the air. By implementing the E20 dry deposition scheme, the CMAQ simulation performance of the surface PM₁₀ has been considerably improved with the NMB of -41.9 %, as compared to the dry deposition proposed by S22 (-47.01 %) and P22 (-53.90 %). The modeled PM₁₀ pattern by E20 at the upper level (700 hPa) was mostly consistent with the observed PM₁₀ at the Lulin Atmospheric Background Station (LABS; 23.47° N, 120.87° E; 2862 m a.s.l.) where is a typical background site at Western Pacific, particularly in capturing the peak value. The correlations (R) at the high-altitude were well performed for E20 by 0.55, as compared to S22 (0.54) and P22 (0.46). Moreover, E20 improved the simulated PM₁₀ concentrations and aerosol optical depth (AOD) value over the Asian Continental during the multiple dust episodes in spring 2021, by NMB of -25.43 % and -26.19 %, respectively. The noticeable deduction of the coarse mode particle's deposition velocity (V_d) was responsible for reducing the PM₁₀ simulation underestimation. On 22-31 January 2023, the *in-situ* measurement of the upper level observed the possibility of natural dust and anthropogenic aerosol. This is consistent with the CMAQ, which shows that both aerosol types displayed a clear "long dust-black

31 carbon belt" along the 15°N. It is revealed that the increase of the surface resistivity (R_b) leads to a
32 significant increase in dust mass concentration but a minor increase in black carbon (BC). We proposed
33 implementing the E20 dry deposition approach, particularly in PM_{10} simulation, narrowing the
34 uncertainty of the CMAQ dust emission treatment.

35 **1 Introduction**

36 The chemical transport model (CTM) is a powerful tool for comprehending air pollution, encompassing
37 emission, transport, radiative impact, and removal mechanisms at various grid scales. Among
38 these, particle dry deposition is a crucial aerosol removal process and an important sink for particles in
39 the model. The derivation of the dry deposition is based on the resistance framework and
40 electrical analogue, but its implementation can vary across models (Wesley, 1989; Giardina and Buffa,
41 2018; Gaydos et al., 2007; Khan and Perlinger, 2017; Shu et al., 2017). A key challenge in dry deposition
42 simulation is the scarcity of measurement data for model verification, underscoring the necessity for
43 further research to enhance the accuracy of air quality modeling.

44 An immense range of dry deposition parameterization has been implanted in the model. The
45 deposition mechanism by Slinn (1982) includes the deposition process such as turbulent transfer,
46 Brownian diffusion, impaction, interception, gravitational settling, and particle rebound, where the
47 particle grows under humid conditions. Zhang et al. (2001) suggested the dry deposition scheme is
48 sensitive to land use category and several parameters. For instance, due to the particle growth, the
49 deposition velocity (V_d) over the ocean is much higher than on another land surface, as the V_d increased
50 rapidly with the increase of particle size. Some CTMs using Zhang et al. (2001) parameterization still
51 underestimated the global $PM_{2.5}$ concentration. The latest dry deposition scheme revision by Emerson et
52 al. (2020) based on the flux measurement of grassland and pine forest has reduced the uncertainty,
53 marking a significant step forward in our quest for more accurate air quality modeling.

54 An updated deposition scheme that reduces the dependence of the deposition velocity on the aerosol
55 mode width has been proposed (Shu et al., 2022). Indeed, the approach suggested that vegetation
56 dependence increased the V_d for submicrons and decreased for large particles by 37 % and -66 %,

57 respectively. It also reduced the functional biases by 56-97 % for vegetated land-use type and equivalence
58 performance over the water. Moreover, adding the second inertial impaction term for microscale obstacles
59 such as leaf hairs, microscale ridges, and needle leaf edge effects managed to increase the mass dry
60 deposition of the accumulation mode aerosols in the model (Pleim et al., 2022). These modifications
61 reduced the average $PM_{2.5}$ in the atmosphere during July 2018 over the contiguous United States.

62 With a plethora of deposition approaches in use, it becomes paramount to comprehend their impact
63 on model performance in predicting aerosol behaviour. The surface fine particle concentrations can vary
64 up to 5-15 %, and the particle dry deposition has more than 200 % discrepancy due to the different dry
65 deposition schemes. (Saylor et al., 2019). A comprehensive evaluation of five different parameterizations
66 has been conducted, with the simplest and most effective deposition mechanism suggested for the CTM
67 (Khan and Perlinger, 2017). However, the model's reliance on meteorological factors such as frictional
68 velocity, relative humidity, rainfall, or wind speed, which can significantly influence
69 the model's accuracy, remains a challenge (Kong et al., 2021).

70 Besides the model bias on $PM_{2.5}$, the simulation of PM_{10} has been underestimated due to the
71 uncertainty of the deposition mechanism, particularly over the western Pacific (Kong et al., 2021). The
72 V_d is overestimated for coarse particles, where the dry deposition velocity is too high for coarse particles
73 when the frictional velocity is large, which is why the surface PM_{10} concentration is underestimated (Ryu
74 and Min, 2022). The model performance of PM_{10} simulation that is widely influenced by the dust
75 treatment embedded within CMAQ has been revised (Dong et al., 2016; Liu et al., 2021; Kong et al.,
76 2021, 2024) and are found to effectively simulate the PM_{10} over the western Pacific region such as
77 Taiwan. However, the issue regarding the deposition algorithm's impact on the model performance at the
78 corresponding region needs to be discussed. The present research intends to evaluate the CMAQ model
79 performance due to the different deposition schemes on aerosols in the Taiwan region.

80 The model performance in Taiwan is paramount in our study, as the area is equipped with a substantial
81 number of well-maintained surface observation sites, providing comprehensive coverage. The LABS
82 station in the high-altitude subtropical western North Pacific region serves as the sole background station

83 for monitoring transboundary pollutants. This station is crucial in our research as it provides unique data
84 on the long-range transport of pollutants, further underscoring the relevance of our study.

85 The transboundary pollutants mechanisms have been widely discussed through LABS measurements,
86 cooperating with the backward trajectory, reanalysis dataset, and modeling approach. Previous research
87 reveals that LABS pollutants could be associated with severe fire emissions from northern Peninsular
88 Southeast Asia (Huang et al., 2020; Ooi et al., 2021) and Indonesia (Ravindra Babu et al., 2023).
89 Moreover, the intense wind speed in northwest China could transport the mineral dust through the surface
90 and high-altitude layer detected at LABS (Kong et al., 2021; Kong et al., 2022). Additionally, the transport
91 process of East Asian haze due to the cold surge from the Asian Continental industrial region towards
92 Taiwan has been widely discussed (Chuang et al., 2020). Instead of pure aerosol, the coexistence of dust
93 and biomass burning over Taiwan, a condition discovered in previous research, has significant
94 implications for the regional climate (Dong et al., 2018; Dong et al., 2019). However, the high-altitude
95 synoptic pattern associated with the coexistence between natural dust and anthropogenic pollutants
96 remains unknown due to a lack of observations at the upper layers.

97 This study used the chemical transport model to investigate the long-range transport of East Asian
98 dust (EAD) that occurred on 22-31 January 2023 and 12 March-20 April 2021. Due to the limitation of
99 the dust model, the CMAQ version 5.4, embedded with three types of dry deposition schemes, was
100 implemented to justify the effectiveness of improving our latest refined dust model (Kong et al., 2024).
101 The dry deposition scheme proposed by Shu et al. (2022) has reduced certain model bias as compared to
102 the base scheme. However, the revised scheme response to the natural phenomenon such as wind-blown
103 dust has not being tested. In the other way, the number of concentrations of the large size particle has
104 been decreased over land, and increased over ocean area globally by the adjusted collective efficiency
105 proposed by Emerson et al. (2020). Pleim et al. (2022) has included the consideration of white cap effect
106 which dependent on wind speed and sea surface temperature into the dry deposition scheme. Hence, the
107 response of the CMAQ dust model under the newly developed dry deposition schemes are worth
108 investigating in reducing the model uncertainty.

LABS detected the recent transboundary episode in January 2023 as a mixing aerosol type (see Section 3.1), which has not been widely discussed, and the multiple dust storm episodes mentioned by Kong et al. (2024) provide an opportunity to model the EAD over the downwind region. Recognizing the significant transboundary events detected through Taiwan's observations, the improvement of the CMAQ dust model by the dry deposition schemes, and its application in characterizing the transport mechanism can be vital. The paper is organized as follows. The model setup and ancillary datasets are discussed in Sect. 2. The results and discussion are presented in Sect. 3, followed by the conclusions in Sect. 4.

2 Data and Methodology

2.1 Dust emission treatment

Before delving into the details, it's important to understand the process of dust transport. Dust is primarily transported by wind through a process known as sandblasting (Kok et al., 2012). For dust to be uplifted, the horizontal wind speed must exceed a certain threshold frictional velocity ($u_{*,t}$), which is estimated by the model as follows:

$$u_{*,t} = u_{*,to} f_m f_r \quad (1)$$

Where $u_{*,to}$ is the ideal threshold friction velocity, while f_m and f_r are the correction factors of soil moisture and surface roughness, respectively.

Through a collaborative effort, the windspeed, soil texture, soil moisture, and surface roughness length derived from field and laboratory studies have been integrated into the windblown dust treatment, which is now a part of the Community Multiscale Air Quality (CMAQ) modeling system (Foroutan et al., 2017). This model, developed and evaluated over the continental United States, has also been extended to the East Asia region (Dong et al., 2016; Liu et al., 2021; Kong et al., 2021, 2024). Kong et al. (2024) have proposed further improvements, including the integration of the revised soil moisture fraction, dust emission speciation profile, and bulk soil density, to enhance the representation of the Asian dust simulation. This ongoing collaboration is crucial for the continuous improvement of our understanding and management of dust emissions.

134 2.2 Particle dry deposition schemes

135 Particle dry deposition is a complex process relating to the deposition velocity, particle size, source and
136 composition, land use surface, and meteorological condition. Generally, the flux of the particle mass
137 through the surface boundary layer is estimated as:

$$138 \quad F = C \times V_d \quad (2)$$

139 where F is the deposition flux, C is the particle concentration at the surface layer, and V_d is the deposition
140 velocity.

141 The difference in the particle concentration and deposition prediction among the various
142 atmospheric chemistry models was probably due to the algorithm of the dry deposition particle. The
143 algorithm describing particle deposition velocity as a function of particle size in almost all current air
144 quality model systems is descended from Slinn (1982). The particle deposition according to vegetative
145 canopies formulated the deposition velocity as:

$$146 \quad V_d = V_g + \frac{1}{R_a + R_b} \quad (3)$$

147 where V_g is the gravitation settling velocity, R_a is the resistivity aerodynamic, R_b is the surface resistivity,
148 also known as quasi-laminar sub-layer resistivity in STAGE. The V_g is calculated according to Stokes's
149 Law as:

$$150 \quad V_g = \frac{p_p D_p^2 g C_c}{18\eta} \quad (4)$$

151 where, p_p is the density of the particle; D_p is the diameter of the particle; g is gravitational acceleration;
152 C_c is the Cunningham correction factor for small particles; and, η is the dynamic viscosity of air.

153 CMAQ is embedded with M3Dry dry deposition calculation that implements the scheme of Pleim
154 and Ran (2011), which is based on Slinn (1982). As noted by Pleim and Ran (2011), chemical surface
155 flux modeling has become an essential process in the air quality model. For instance, the linkages of

156 ambient concentration levels to the deposition of SO_x and NO_x. Moreover, Surface Tiled Aerosol and
157 Gaseous Exchange (STAGE) deposition has been implemented within the CMAQv5.3, where estimated
158 fluxes from sub-grid cell fractional land-use values, aggregate the fluxes to the model grid cell and unifies
159 the bidirectional and unidirectional deposition schemes using the resistance framework (Massad et al.,
160 2010; Nemitz et al., 2001). The updated STAGE version in CMAQv5.4 could aggregate the grid-scale
161 values that match the grid-scale values from most kinds of Land Surface Model of WRF (Hogrefe et al.,
162 2023). Since the present study is primary focused on the impact of dry deposition scheme on CMAQ dust
163 modeling, the simulations with the STAGE module are the mandatory concern (Table 1).

164 **2.3 CMAQ model design**

165 This study applied WRF v4.0 for the meteorological field parameters and CMAQv5.4 to simulate the
166 transboundary East Asian dust episodes on 22-31 January 2023, and the multiple dust storm episodes
167 during 12 March-20 April 2021. The modeling domain was set up to cover the Taklamakan and Gobi
168 Desert, with a resolution of 45 km, and nested towards Taiwan at a resolution of 15 km (d02) and 5 km
169 (d03) (Fig .1, Table 2). Also, as Taiwan is influenced by biomass burning, the domain covers up to the
170 peninsular Southeast Asia (PSEA), which will be carried out in the future (Ooi et al., 2021). The model
171 consisted of 40 vertical layers, with eight layers below ~1 KM altitude, 13 layers below ~3 KM altitude,
172 and 27 layers covering the upper layer to ~21 KM. The model's initial and lateral boundary
173 conditions were constructed using the National Centers for Environmental Prediction (NCEP) Final
174 Analyses (FNL) reanalysis dataset on a 0.5° × 0.5° grid. The data assimilation was conducted by grid
175 nudging in all the domains. The CB06 gas-phase chemical mechanism and the AERO7 aerosol module
176 model were implemented in CMAQ for the present study.

177 The anthropogenic emission inventories in East Asia, crucial for our research, were obtained from
178 the MICS-Asia (Model Inter-Comparison Study for Asia) Phase III emission inventory (Li et al., 2017).
179 The emissions of SO₂, NO_x, NMVOC, NH₃, CO, PM₁₀, PM_{2.5}, BC, OC and CO₂ has been meticulously
180 modified, taking into account of the relative changes in China's anthropogenic emissions between 2010
181 and 2017 (Zheng et al., 2018). Additionally, the modified emission of NO₂ was adjusted further by the
182 satellite imagery OMI-NO₂ in January 2023 (Huang et al., 2021). Biogenic emissions for Taiwan were

183 prepared by the Biogenic Emission Inventory System version 3.09 (BEIS3, Vukovich and Pierce, 2002)
184 and, for regions outside Taiwan, by the Model of Emissions of Gases and Aerosols from Nature v2.1
185 (MEGAN, Guenther et al., 2012). TEDS 10.0 (Taiwan Emission Database System, TWEPA, 2011;
186 <https://erdb.epa.gov.tw/>, last access: 18 January 2024) was used for domain 3 (d03). To ensure the
187 precision of the multiple dry deposition parameterizations, the present research conducted four simulation
188 scenarios, namely CMAQ_Off_S22, CMAQ_Dust_S22, CMAQ_Dust_E20 and CMAQ_Dust_P22. The
189 CMAQ_Off_S22 scenario did not include the inline dust calculation (Table 3). Meanwhile, the latest
190 refined integrated dust treatment was implemented in the CMAQ_Dust_S22 scenario (Kong et al., 2024).
191 Indeed, both CMAQ_Off_S22 and CMAQ_Dust_S22 used the dry deposition mechanism by Shu et al.
192 (2022). The dry deposition mechanism of Emerson et al. (2020) and Pleim et al. (2022) were implemented
193 in CMAQ_Dust_E20 and CMAQ_Dust_P22 scenarios, respectively.

194 V_d over the ocean surface has been shown to influence the CTMs in simulating aerosol,
195 particularly PM_{10} . The modeled PM_{10} can be increased by reducing V_d by a factor of 10 based on the bare
196 soil measurement (Tav et al., 2018; Ryu et al., 2022). However, the adjusted V_d in estimating the aerosol
197 was too coarse. In Eq. (3), the parameterizations of R_a and R_b determined the magnitude of V_d . P22 dry
198 deposition scheme in CMAQv5.4 includes the white-cap effect over the ocean surface, which is related
199 to the particle collection efficiency by impaction, as a function of R_b (Pleim et al., 2022). The impact of
200 the white cap can increase as the wind speed increases, which can be an essential parameterization in
201 simulating transboundary events (Albert et al., 2020). Our findings on dust transport, which was highly
202 related to turbulence, have significant implications for future research and modeling, inspiring further
203 exploration and innovation (Zhang et al., 2022). In CMAQv5.4, R_b is estimated separately by vegetation
204 and non-vegetation type. R_b at the smooth surface (non-vegetation) is related to the surface resistivity of
205 the bare soil and the water layer. Since EAD aerosol particles are mostly uplifted from the bare soil surface
206 layer and the aerosol deposition at the marine boundary layer (Kong et al., 2021), the sensitivity of R_b at
207 the smooth surface impact on the CMAQ dust model simulation can be vital. By assuming $R_b = 1/V_d$, V_d
208 is inversely dependent on R_b , we increased R_b to a factor of 10 as P22E01. To further carry out the
209 sensitivity test, we scale R_b by 50 and 100, for P22E02 and P22E03, respectively (Table 3).

210 **2.4 Ancillary dataset**

PM₁₀ (particulate matter ≤ 10 μm in aerodynamic diameter) and PM_{2.5} (particulate matter ≤ 2.5 μm in aerodynamic diameter) concentrations during the dust events in January 2023 were obtained from Lulin Atmospheric Background Station (LABS; 23.47° N, 120.87° E, 2862 m MSL) and Cape Fuguei (25.30° N, 121.54° E, 10 m MSL). In addition, the hourly PM₁₀ and PM_{2.5} of nearly 100 sites distributed over mainland China (Fig. S1), covering the period of 12 March-20 April 2021, obtained from the Chinese air quality online monitoring analysis platform's website (www.aqistudy.cn/). The Modern Era Retrospective-analysis for Research and Application version 2 (MERRA-2) reanalysis data was used to demonstrate the spatiotemporal distribution of dust, compare with the air quality model, irrespective of the influence of clouds. MERRA-2 (Gelaro et al., 2017) is a NASA reanalysis utilizing Goddard Earth Observing System Data Assimilation System Version 5 (GEOS-5) and covering the data assimilated system at a native spatial resolution of $0.5^\circ \times 0.625^\circ$. Also, Moderate Resolution Imaging Spectroradiometer (MODIS) Terra satellite images and the level-3 MODIS AOD at 550 nm (MYD08) were obtained from the U.S. National Aeronautics and Space Administration (<https://worldview.earthdata.nasa.gov/>).

3 Results and Discussion

3.1 Observed air quality and weather conditions

Figure 2 shows the dust outbreak over East Asia, displayed by the MODIS Terra sensor and MODIS AOD at 550 nm from 22-31 January 2023. The satellite image showed dust induced by a high-pressure system on 24-25 January (Fig. 2a3, 2a4). The next day, the same region was covered by a thick cloud, and dust was again widely distributed from 27-30 January 2023. Using MODIS AOD to verify the dust plume (Han et al., 2012; Kong et al., 2021), the dust plume was distributed in Central China and northern Taiwan on 24 January 2023. Moreover, the most intense dust plume in the eastern China and East China Sea region was observed on 27 January. Fig. S2 shows the synoptic weather map across the study domain. On 22-23 January, the southward high-pressure system was responsible for pushing the pollutant across the Asian Continent, which is consistent with Chuang et al. (2018) and Kong et al. (2021, 2022, 2024) (Fig. S2a-b). The high-pressure system that moved southward will then move eastward toward the western

237 Pacific Ocean (Fig S2c-d). Meanwhile, the high-pressure system on the northwest side again expands in
238 the southeast direction. The second high-pressure system again pushed the pollutant for the second time
239 and caused the high pollutant problem on 27 January.

240 The impact of East Asian dust on the air quality over the high-altitude western Pacific region was
241 widely discussed (Kong et al., 2022). Two interesting high pollution events at Mt. Lulin (2,862 m above
242 sea level) during 24-26 Jan and 27-30 January, respectively, are shown in Fig. 3. The latter event was
243 more intense compared to the earlier one, where the maximum PM₁₀ concentration can reach up to 35 µg
244 m⁻³. Moreover, it was observed that the BC concentrations could reach up to a maximum of 400 ng m⁻³.
245 Based on the *in-situ* measurement, it was interesting to find the mixing state between dust, BC, and brown
246 carbon (Fig. 3c). Different from what has been discussed by Kong et al. (2022), the long-range transport
247 air pollution at the high-altitude not just merely EAD, but also included the anthropogenic pollutant from
248 mainland China.

249 **3.2 Evaluation of CMAQ dust emission and dry deposition parameterizations**

250 Table 4 shows the statistical analysis of PM₁₀ and PM_{2.5} concentrations over Cape Fuguei (northern
251 Taiwan) from 22-31 January under the multiple deposition mechanisms. The threshold of the statistical
252 index is based on Emery (2001). CMAQ_Off_S22, the PM₁₀ simulation presented without the inline dust
253 calculation, recorded the normalized mean bias (NMB) of -52.81 %. CMAQ_Dust_S22 improved the
254 simulation over Cape Fuguei (northern Taiwan) by -47.01 % as we included the refined dust treatment
255 (Kong et al., 2024). However, the improvement is insignificant due to the weak intensity dust episodes
256 and the limitation due to the excessive deposition mechanism within the model (Kong et al., 2021). Hence,
257 we expanded the sensitivity simulation to examine the impact of the deposition algorithm on the aerosol
258 prediction. CMAQ_Dust_E20 simulations utilizing the Emerson et al. (2020) approach increased the
259 modeled PM₁₀ simulation by NMB of -41.9 %.

260 Instead of PM₁₀ simulation, the present study found that the inline dust treatment and deposition
261 algorithms could influence PM_{2.5} simulation performances. For instance, the modeled PM_{2.5} improved
262 from -12.63 % (CMAQ_Off_S22) to -8.84 % (CMAQ_Dust_S22). Meanwhile, the deposition algorithm

263 embedded in CMAQv5.4 has recorded modeled $PM_{2.5}$ by -10.65 % and -15.22 % under
264 CMAQ_Dust_E20 and CMAQ_Dust_P22, respectively. This incident suggested that the East Asian dust
265 from northwest China transported to the Western Pacific Ocean could also carry the anthropogenic
266 emission of East China.

267 Figure 4 shows the time series of hourly PM_{10} and $PM_{2.5}$ concentrations over Cape Fuguei
268 (northern Taiwan) and LABS (high altitude region) from 22-31 January 2023 under the multiple
269 deposition mechanisms. Generally, all the patterns of PM_{10} simulations were consistent with the observed
270 PM_{10} , especially in capturing the peak value. For instance, the maximum observed (CMAQ_Dust_E20)
271 PM_{10} concentrations at the surface during Jan 24 and 27 were 141 (102.6) $\mu g m^{-3}$ and 114 (163.2) $\mu g m^{-3}$,
272 respectively. A similar time-series pattern was found for the $PM_{2.5}$ simulation (Fig. 4b).

273 More importantly, the CMAQ model performance over the high-altitude region needed to be
274 carried out and discussed. The biomass-burning episode of the northern PSEA over Mt. Lulin has been
275 finely correlated by plume rise injection (Chuang et al., 2016; Ooi et al., 2021). From Fig. 4c, the modeled
276 PM_{10} pattern for CMAQ_Off_S22 could not correlate well with observed PM_{10} over Mt. Lulin, with a
277 poor correlation of 0.30. The correlation was increased for CMAQ_Dust_S22 (0.54), CMAQ_Dust_P22
278 (0.46), and primarily well performed for CMAQ_Dust_E20 (0.55). The modeled result
279 was somehow consistent with the surface PM_{10} simulation at Cape Fuguei. The high observed PM_{10}
280 episodes during 27-28 January with a maximum of 34.5 $\mu g m^{-3}$ was only 53.3 % higher than
281 CMAQ_Dust_E20 of 22.5 $\mu g m^{-3}$. For the CMAQ $PM_{2.5}$, the simulation generally underestimated the
282 observed $PM_{2.5}$. It's worth noting that E20, in particular, showed exceptional performance in the PM_{10}
283 simulation compared to other dry deposition schemes under the refined dust scheme. This underscores
284 the potential effectiveness of E20 in managing PM_{10} particulate matter. However, the $PM_{2.5}$ simulations
285 showed only marginal changes, regardless of whether it was a surface or high-altitude simulation.

286 During the spring of 2021, a series of dust storms (15 March, 27 March, and 18 April) occurred
287 over the Gobi area, with one of the most significant dust storms in the past decade (15 March, the “3.15”
288 dust storm hereafter) causing environmental impact over the continental (Jin et al., 2022; Gui et al., 2022;

289 He et al., 2022; Liang et al., 2022; Tang et al., 2022). More interestingly, one of the multiple dust storm
290 episodes reached western Pacific Ocean due to the extreme typhoon episode (Kong et al., 2024). Hence,
291 we intend to re-emphasize the precision of various deposition schemes on the CMAQ for the recent dust
292 storm episode over the Asian Continental highlighted by Kong et al. (2024). We evaluated the CMAQ
293 simulations with the different dry deposition schemes for the 40-day sensitivity test on 12 March-20 April
294 2021 against measured PM_{10} and $PM_{2.5}$ concentrations across the observation sites in mainland China
295 (Table 5). The observation sites used for the model comparison are marked in Fig. S1. Generally, the
296 evaluation results for Taiwan and mainland China were consistent. During the 40 days of Spring 2021,
297 the CMAQ PM_{10} of NMB was the highest for Off_S22 (NMB = -75.00 %), followed by Dust_S22 (-45.97
298 %). The latest inline dust emission scheme embedded with E20 dry deposition scheme for PM_{10} was well
299 performed by NMB of -25.43 %, compared to the Dust_P22 (-59.82 %). For the $PM_{2.5}$ simulation,
300 Dust_S22 has been improved from Off_S22, and Dust_S22 was slightly better than Dust_E20 and
301 Dust_P22.

302 Figure 5 shows the scatter plot of simulated and observed PM across mainland China. The
303 correlation coefficient (R), a factor of two (FAC2), and the mean observed and simulated PM are marked
304 in Figure 5. The modeled PM_{10} without the dust scheme had the lowest correlation. Among all of these
305 simulations, Dust_E20 performed the best correlation ($R > 0.3$) compared to Dust_S22 and Dust_P22.
306 However, for $PM_{2.5}$, the correlation between the model and measured values was similar for all the dry
307 deposition schemes. The statistical index of FAC2 was used in the present work since either low or high
308 outliers less influence it (Chan and Hanna, 2004). The dataset is reliable for FAC2 values between 0.5
309 and 2.0, with the ideal model of 1.0. The simulated PM_{10} by Dust_E20 performed well, with a nearly
310 perfect value of 1.1. Meanwhile, the $PM_{2.5}$ by Dust_S22 simulation was slightly better than Dust_E20 but
311 much better than the other experiments.

312 The comparison of AOD between CMAQ and MODIS for the three dust storm episodes: 14-16
313 March 2021 (“3.15” dust storm), 26-28 March 2021 (“3.27” dust storm), and 17-19 April 2021 was shown
314 (“4.18” dust storm) (Table 5). Overall, CMAQ Dust_E20 above 30°N has evaluated well the MODIS
315 AOD by NMB of -26.2 %, as compared to S22 (-32.0 %) and P22 (-35.8 %). The CMAQ AOD by E20

316 during the most intense Super Dust Storm in 3.15 has significantly improved over northern China, the
317 dust source region, as shown in the red dash rectangular box (Fig. S3). Additionally, the modeled AOD
318 by E20 over the western Pacific Ocean (shown in red dash rectangular box) increased in episode 4.18,
319 reporting a value of 0.7 compared to 0.5 by S22. Significantly, the E20 deposition scheme has primarily
320 enhanced the PM₁₀ prediction over the marine boundary layer, addressing the model uncertainty due to
321 the typhoon mentioned by Kong et al. (2024) and demonstrating the practical implications of our research.

322 The present work is consistent with the dust scheme in the WRF-Chem, where the dust loading is
323 very sensitive to the dry deposition schemes and dust emission schemes, especially over the downwind
324 region (Zeng et al., 2020). Fig. 6 shows the CMAQ estimated averaged mean PM₁₀ and PM_{2.5} in January
325 2023 and Spring 2021 for the Off_S22 and its corresponding change by Dust_S22, Dust_E20, and
326 Dust_P22, respectively. Generally, the spatial distribution of the high PM₁₀ concentrations by $> 50 \mu\text{g m}^{-3}$
327 was distributed over northwest China, which is the dust source region's location, consistent with the
328 simulation suggested by Kong et al. (2021, 2022, 2024). Such high particulate matter dissipated to east
329 China, indicating the transport pathway in the southeastern direction towards the western Pacific (Fig. 6a,
330 h). The larger PM₁₀ distribution by E20 than S22 and P22 over northwest China, meaning E20
331 successfully increased the PM₁₀ concentrations. Another fascinating fact about E20 was that the PM₁₀
332 increased over the southern South China Sea (Fig. 6b). For the modeled PM_{2.5} concentrations, the high
333 concentration was distributed over the Asian Continental under all dry deposition mechanism. Similar to
334 the trend of PM_{2.5} simulations in Taiwan (as shown in Fig. 4), the spatial distribution of the modeled
335 PM_{2.5} was identical to that of all dry deposition schemes. The result implies the significant impact of dry
336 deposition on the EAD simulation's dust model, displaying the positive relationship between dust
337 deposition and PM₁₀ concentrations (Zhang et al., 2017).

338 3.3 Impact on the CMAQ ambient particle concentrations

339 Figure 7a shows the boxplot of the averaged simulated V_d for the Aitken, accumulation, and coarse
340 particles modes under multiple deposition schemes in January 2023 (S22_2023, E20_2023, and
341 P22_2023) and in Spring 2021 (S22_2021, E20_2021, and P22_2021). These different dry deposition

342 treatments have a substantial impact on the aerosol profile, altering the ambient total dry deposition
343 regionally. For instance, the median deposition velocity of S22_2023, E20_2023, and P22_2023 of the
344 Aitken (accumulation) modes particle were 0.069 (0.020) cm s^{-1} , 0.039 (0.014) cm s^{-1} and 0.034 (0.029)
345 cm s^{-1} , respectively. The E20 simulation median V_d decreased by -12.65 % for coarse-mode particles
346 compared to S22. Also, the 75th percentile V_d of the coarse mode has been significantly reduced by -32.13
347 %. On the other hand, P22 showed a different simulation by the median V_d increment of 71.38 %. These
348 findings suggest that the choice of dry deposition treatment can significantly influence the distribution
349 and concentration of aerosols in the atmosphere, with potential implications for air quality and climate.

350 As shown in Figure 7a, the results during the spring of 2021 are similar to those for January 2023
351 in comparing the dry deposition schemes. Notably, the V_d of the coarse mode for E20_2023 and
352 E20_2021 was lowest compared to the other dry deposition schemes. Contrary, the accumulation and
353 coarse mode by P22 were the highest. The result was consistent with the best simulated PM_{10} by E20 in
354 2023 and 2021 displayed in Table 4 and 5, respectively. The lowest V_d of the coarse mode particle was
355 responsible for reducing the PM_{10} simulation underestimation, consistent with the simulation by Ryu and
356 Min (2022). The slow V_d means the total loss of aerosol to the surface has been minimized, leading to
357 increased aerosol concentration. In addition, the spatial distribution of dust emissions could significantly
358 influence the aerosol deposition velocity. The total dust emission in Spring 2021 was of a much higher
359 magnitude and wider spatial distribution than in January 2023 (Fig. 7b, c). This led to a slow V_d in the
360 coarse mode, particularly, causing more dust loading during the multiple dust storms in Spring 2021 than
361 the regular dust episode recorded in January 2023. This finding is consistent with Zeng et al. (2020),
362 which emphasized the sensitivity of different dust emissions on dry deposition schemes. However, it's
363 important to note that the research was only conducted in one particular short period. On the other hand,
364 this work has highlighted the distinct dust emission according to EAD intensity impacting the various dry
365 deposition schemes. These implications are crucial for understanding the behaviour of aerosols in the
366 atmosphere and their significant impact on air quality.

367 We estimated the CMAQ averaged particle modes for the S22_2023, E20_2023, and P22_2023
368 dry deposition scheme (Fig. 8). For S22_2023, we found that high V_d corresponding to the Aitken and

369 accumulation modes distributed mainly over most of the CMAQ domain, which was most evident over
 370 Asian continent (Fig 8a, 8d). Meanwhile, the magnitude of V_d distribution was the most significant over
 371 the western Pacific Ocean by S22_2023 and the least for E20_2023 (dash rectangular box in Fig. 8d, e,
 372 f). For the coarse mode particles, the V_d was the lowest for E20_2023 compared to S22_2023 and
 373 P22_2023, particularly over the ocean area near northeast China, Japan, and Korea (white-dash
 374 rectangular box in Fig. 8d, e, f). This leads to a significant deposition over the downwind region, causing
 375 less PM_{10} simulated by P22_2023 and S22_2023 than E20_2023. A previous study proposed the V_d for
 376 the aerosol at the water surface was associated with the CTM uncertainty at the downwind region (Kong
 377 et al., 2021, 2024; Ryu and Min, 2022). The V_d at land surface was generally higher than at water surfaces.
 378 Interestingly, the coarse mode V_d at the water surface for E20_2023 (0.060 cm s^{-1}) was lower than
 379 S22_2023 (0.085 cm s^{-1}) and P22_2023 (0.116 cm s^{-1}), respectively, suggesting that E20_2023 deposition
 380 schemes could minimize the excessive deposition over the marine boundary layer (Table 6). Such minimal
 381 deposition velocity distributing over a large part of the western Pacific Ocean, including the Sea of Japan,
 382 Yellow Sea, East China Sea, and South China Sea, might be responsible for reducing the modeled PM_{10}
 383 underestimation over Taiwan (Fig. 8h), as mentioned by Kong et al. (2021).

384 To better understand the behavior of the V_d during the 40-day simulation of Spring 2021
 385 corresponding to the aerosol simulation, we visualized the CMAQ averaged particle modes for the
 386 S22_2023, E20_2023, and P22_2023 dry deposition scheme (Fig. 9). The V_d of the coarse mode particles
 387 for E20_2021 was the lowest among the others over the ocean area, which shows similarity as E20_2023
 388 (Fig. 9g, h, i). As mentioned by Kong et al. (2024), one of the continuous EAD episodes was related to
 389 the typhoon. The strong wind speed and extreme precipitation due to the intense anticyclonic system
 390 caused nearly zero dust simulation. In S22_2021 (0.060 cm s^{-1}) and P22_2021 (0.070 cm s^{-1}), the model
 391 suggested high coarse mode V_d at the western Pacific Ocean. In E20_2021, the V_d (0.053 cm s^{-1}) is lower
 392 than the rest of the dry deposition mechanism, particularly the area affected by typhoon (black-dash
 393 rectangular box). This means that the E20 dry deposition has reduced the uncertainty of the excessive
 394 dust loss at the marine boundary layer. Figure 6 (g, h, i) shows more simulated mineral dust at the western
 395 Pacific by E20 than S22 and P22 during the spring of 2021.

396 3.4 CMAQ of dust and black carbon synoptic pattern at the upper level

397 Black carbon (BC), often known as elemental carbon, released from the biofuels, fossil fuels and biomass
398 burning, has been proven to impact the radiative budget and regional climate (Ramanathan, V and
399 Carmichael, 2008; Pani et al., 2016, 2020). In the meantime, China has been a significant contributor to
400 global anthropogenic BC emission, particularly in the cities of the northern part (Xiao et al., 2023; Wang
401 et al., 2024). During the severe dust episodes in the spring of 2023, the contribution of black carbon
402 brought by EAD was captured in North China (Wang et al., 2024). As depicted in Fig. 2, the
403 transboundary episode observed in the upper level of Taiwan during this event could be the mixing of the
404 natural dust and anthropogenic haze episodes, which demonstrates the consistency. Additionally,
405 blending mineral dust with anthropogenic transport due to the north easterly wind, a wind that blows from
406 the northeast, has been a subject of extensive discussion (Lin et al., 2007, 2012; Li et al., 2012). During
407 the EAD, the dust from the Gobi Desert that was transported towards the western Pacific region could
408 also carry anthropogenic aerosol, contributing to different levels of pollutant concentration. However, the
409 distinct transport pathway at the high altitude between both aerosol types is a topic that has received less
410 attention but is of significant importance to our understanding of atmospheric dynamics.

411 Figure 10 illustrates mineral dust and BC concentration's spatial and temporal distribution under
412 the CMAQ_Dust_E20 scenario at 700 hPa from 24-31 January. The model reveals a high proportion of
413 modeled dust aerosol (red dash circle) at the source region, indicating an uplift from the surface to 700
414 hPa (Fig. 10a). This uplift, driven by the strong pressure gradient at the surface and the 'eastward moving
415 trough system' at the upper level (700 hPa), is a key factor in the eastward and southward transfer of the
416 dust (Fig. 10b). The high dust fraction reappears at the source region (Fig. 10c) and is transported
417 eastwardly by the similar upper-level trough (Fig. 10d), causing a long dust belt at 15°N, distributing over
418 central Asia continental, Taiwan Straits, Taiwan and large part of western Pacific Ocean. (Fig. 10e). On
419 29 January, the model of E20 clearly predicted that the dust plume moved in the southward direction
420 toward the South China Sea (Fig. 10f). The dust aerosol was left distributed at a certain part of the northern
421 South China Sea and the Philippine Sea until it totally dissipated (Fig. 10g, h). This interesting result

422 suggests the possible EAD at the longer distance at the upper level, which is a topic for further
423 investigation.

424 The southward high-pressure system responsible for the long-range transport haze episode has
425 been widely discussed (Chuang et al., 2008; Kong et al., 2021)—however, the upper-level transboundary
426 transport needs to be addressed more. While focusing on CMAQ_Dust_E20, we attempted to characterize
427 the long-range transport of modeled black carbon at the upper level (700 hPa) (Fig. 10i-p). As shown in
428 Fig. 10(i), the modeled black carbon concentration is shown to be significantly distributed at central
429 China. The black carbon transport pattern followed the eastward-moving trough system as the plume
430 moved eastward and southward (Fig. 10m, n). Interestingly, the long black carbon belt is consistent with
431 the long dust belt, as shown in Fig. 10(e, f). For instance, both modeled dust and BC were distributed at
432 the western Pacific Ocean (Fig. 10e, f, m, n) and South China Sea (Fig. 10g, o). This means that the BC
433 due to the anthropogenic emission and the natural EAD shared a similar transport pattern at the upper
434 level, driven by the trough system. Such consistency has been verified by the MERRA-2 dust and BC
435 mass column over the region (red dash rectangular in Fig. S4).

436 The dust aerosol vertical profiles (Fig. 11) show a significant distribution of the large dust fraction
437 over the Asian Continent under all simulation scenarios (Fig. 11a1-e1), as indicated by the transect drawn
438 in Fig. 1. The westerly winds, depicted in Fig. 10, facilitated the eastward transport of the aerosol plume
439 towards the western Pacific Ocean, where it accumulated along the 700 hPa altitude. Another plume was
440 observed across the ocean on the east side of Taiwan Island (Fig. 11b1). On 27 January, showed another
441 substantial fraction of dust covering the Asian Continent and Western Pacific Ocean, with significantly
442 higher dust concentrations compared to Fig. 11a1. The plume distributed eastward exhibited a clear dust
443 dome (Fig. 11a5-e5). These findings have important implications for understanding and predicting dust
444 aerosol transport patterns and their potential environmental impact.

445 The vertical profile of the modeled BC mirrors the transport pattern of mineral dust, as shown in
446 Fig. 12. A transparent BC dome was distributed along 700 hPa, echoing the pattern observed for dust.
447 This simulation suggests the consistency of the “double dome” mechanism of Asian dust and biomass

burning episodes (Dong et al., 2018; Huang et al., 2019). The potential warming effect of such a mechanism is a topic ripe for future studies. However, it's important to note that the dust dome contains a higher fraction of concentrations than the black carbon dome. The present simulation suggests that dust aerosol can reach up to 500 hPa, which is consistent with Kong et al. (2021). On the other hand, the black carbon plume was slightly lower, with approximately 600 hPa of the maximum height under the same meteorological condition. This section, which discusses the similarity and distinctiveness of natural dust and anthropogenic aerosol at the upper level, highlights the need for further study. The present simulation did not consider the two-way coupling model, and it is strongly suggested for future research.

Table 7 shows the modeled deposition and mass concentration for different simulation scenarios in January 2023. The simulation of the wet deposition and mass concentration for dust aerosol was the highest by E20. This is consistent with the globally averaged aerosol number concentrations over the ocean for the large size particle (Emerson et al., 2020). Contrary, P22 was the lowest in simulated wet deposition and mass concentration. P22 could increase the accumulation mode's V_d and reduce the $PM_{2.5}$ over CONUS, which is similar to the present result (Pleim et al., 2022). Moreover, the present simulation by P22 showed the highest V_d of the coarse mode that leads to the less simulated PM_{10} . P22 revised the impaction collective efficiency, which is the parameterization of R_b . In order to understand the sensitivity of R_b on CMAQ simulation, the R_b has been scaled up, as shown in Table 3. Generally, the increment of R_b has gradually increased the wet deposition (surface mass concentration) by 13.6 (45.8) %, 25.2 (83.3) %, and 28.2 (93.7) %, under P22E01, P22E02 and P22E03, respectively. In addition, the increment intensity at the surface was higher than at the upper level. The simulated dust at western Pacific Ocean responding to the different dry deposition schemes was shown during 27 January in Figure 11 (red-dash rectangular box). As R_b increased by P22E01 and P22E03, the simulated PM_{10} by base scheme P22 ($\sim 30 \mu g m^{-3}$), has increased to $\sim 40 \mu g m^{-3}$ and $\sim 50 \mu g m^{-3}$, respectively. It is worth noted that P22E03 simulated a similar dust concentration as E20, indicating the importance of revising the R_b . On the contrary, the wet deposition and mass concentration were most significant for modeled BC under the S22 dry deposition scheme (Table 7). P22E01 only showed a minor increment, but it was nearly identical for P22E02 and P22E03 compared to P22.

475 **4.0 Summary and Conclusions**

476 The chemical transport model is considered sensitive to the dry deposition parameterization besides the
477 dust emission treatment. The present study demonstrates the impact of the dry deposition
478 parameterizations (S22, E20, and P22) on aerosol performance in East Asia. It provides a significant
479 analysis of the transboundary transport of East Asian Dust to Taiwan from a 22-31 January 2023 case
480 study and multiple heavy dust storm episodes from 12 Mar-20 Apr 2021. Incorporating the latest dust
481 emission treatment (Kong et al., 2024) into the CMAQ slightly improved the model performance to -
482 47.01 % from -52.81 %. By implementing the E20 dry deposition scheme, characterized by calibrating
483 the collection efficiency by Brownian diffusion and interception, the CMAQ simulation of the surface
484 PM_{10} has been improved by NMB of -41.9 %, as compared to the dry deposition proposed by P22 (-53.90
485 %). Moreover, the modeled PM_{10} pattern by E20 at the upper level (700 hPa) was mainly consistent with
486 the observed PM_{10} , especially in capturing the peak value. The dry deposition of E20 was correlated well
487 with the high altitude in situ by 0.55, as compared to S22 (0.54) and P22 (0.46). On the contrary, simulated
488 surface $PM_{2.5}$ by S22 has been improved to -8.84 % from -12.63 % after using the latest dust treatment,
489 and slightly better performance than E20 (-10.65 %) and P22 (-15.22 %). Additionally, the simulations
490 of the multiple dust episodes in spring 2021 were re-constructed to evaluate the CMAQ performance over
491 the Asian Continental. The E20 dry deposition scheme outperformed the others with the lowest NMB
492 value in simulating PM_{10} (-25.4 %) and AOD (-26.2%). For the modeled $PM_{2.5}$, S22 performed slightly
493 better than E20, with NMB of -36.29 % and -37.5 %, respectively.

494

495 The previous CMAQ model, modulated by Kong et al. (2021; 2024), showed excessive deposition at the
496 marine boundary layer, leading to underestimating the modeled surface PM_{10} . However, using the E20
497 scheme over the entire model domain, our updated model has the lowest V_d . This precise reduction of V_d
498 of the coarse mode particle, responsible for reducing the PM_{10} simulation underestimation, has not just
499 minimized, but effectively minimized the total loss of aerosol to the surface, leading to a concentration
500 increment. Furthermore, the low-lying modeled V_d across the water surface by E20 could be crucial in
501 reducing the excessive aerosol deposition over the ocean layer.

502

503 It is worth revealing that the transboundary transport of EAD from the Asian continent towards the
504 western Pacific Ocean at the upper level was associated with the eastward moving trough system. Such
505 transport mechanisms have been found to bring along black carbon aerosol, which is primarily the main
506 element of China's human-made emissions. More interestingly, both aerosol profiles created a "long dust-
507 black carbon belt" along the 15°N. The 'double dome mechanism', a concept proposed by Huang et al.
508 (2019) that depicts the superposition of the two aerosol types, was also simulated in the present study.
509 Besides the similarity of both, the discrepancy in the case of the aerosol deposition and mass concentration
510 was shown. By comparing the base P22 scheme to the revised scheme (P22E01-P22E03), the dust aerosol
511 increased significantly and marginally by the black carbon. This study highlights the importance of dry
512 deposition schemes for the modeled dust and black carbon concentration and provides a reference for
513 better dry deposition schemes in CTMs over East Asia.

514

515 We noted that the improved model simulation for EAD relied on dust emission, dust deposition, and
516 transport processes. The dust emission treatment was proven sensitive to the CMAQ model performance
517 in East Asia (Dong et al., 2018; Liu et al., 2021; Kong et al., 2024). In addition, the CTM performance
518 can be attributed to the dust emission schemes and the dry deposition schemes (Zeng et al., 2020). In
519 other words, different dust emission schemes may impact the V_d and dust loading, which reacts differently
520 to model performance. The present research, which is a complex examination, is of significant importance
521 as it primarily focuses on which dry deposition scheme can improve the most recent updated dust emission
522 model. Therefore, the sensitivity of the dust emission parameterizations or approaches, including surface
523 roughness, land surface, soil texture, and types on the dry deposition scheme, underscores the need for a
524 comprehensive understanding and is proposed for future studies.

525

526 Finally, it is necessary to point out that the dry deposition on the EAD is closely associated with the PM_{10}
527 concentration (Zhang et al., 2017). Nevertheless, it has been shown that there are other atmospheric
528 processes related to the air quality over the Western Pacific, including transboundary haze, biomass
529 burning, and local emission (Chuang et al., 2020; Ooi et al., 2021; Chang et al., 2023). These complex
530 phenomena could cause variations of $PM_{2.5}$, ozone, and the corresponding primary pollutant. Hence, the

531 role and response of the dry deposition scheme in the CMAQ should be paid attention to in the future for
532 compressive understanding and model improvement. This research enhances our understanding of dust
533 emission and dry deposition models and provides valuable insights for improving air quality models,
534 which is crucial for environmental and public health management.

535 **Data Availability**

536 MERRA-2 data are available online through the NASA Goddard Earth Sciences Data Information
537 Services Center (GES DISC; <https://disc.gsfc.nasa.gov>; last access: 01 August 2024). MODIS data used
538 in this study are available at <https://asdc.larc.nasa.gov/>(last access: 01 August 2024). The observational
539 data at LABS can be ordered by contacting corresponding authors.

540 **Author Contribution**

541 **Steven Soon-Kai Kong:** Conceptualization; Data curation; Formal analysis; Investigation; Methodology;
542 Software; Validation; Visualization; Writing – original draft; Writing – review and editing.

543 **Joshua S. Fu:** Conceptualization; Investigation; Methodology; Formal analysis; Writing – review and
544 editing.

545 **Neng-Huei Lin:** Conceptualization; Visualization; Supervision; Funding acquisition; Resources; Writing
546 – review and editing.

547 **Guey-Rong Sheu:** Funding acquisition; Resources.

548 **Wei-Syun Huang:** Data curation; Software.

549 **Competing Interests**

550 Some authors are members of the editorial board of journal ACP.

551 **Acknowledgments**

552 We acknowledged the National Science and Technology Council of Taiwan, under Project No.
553 NSTC113-2811-M-008-045 for supporting the research. We also acknowledged the staff at LABS, and
554 EPA Taiwan for the provision of the ground-based measurement datasets. We are also thankful to
555 MERRA-2 and MODIS for the satellite product.

556 **References:**

557 Albert, M. F., Anguelova, M. D., Manders, A. M., Schaap, M., & Leeuw, G. D.: Parameterization of
558 oceanic whitecap fraction based on satellite observations. *Atmospheric Chemistry and Physics*, 16, 21,
559 13725–13751. <https://doi.org/10.5194/acp-16-13725-2016>, 2016.

560 Chang, J. H.-W., Griffith, S. M., Kong, S. S.-K., Chuang, M.-T., and Lin, N.-H.: Development of a
561 CMAQ–PMF-based composite index for prescribing an effective ozone abatement strategy: a case study
562 of sensitivity of surface ozone to precursor volatile organic compound species in southern Taiwan, *Atmos.*
563 *Chem. Phys.*, 23, 6357–6382, <https://doi.org/10.5194/acp-23-6357-2023>, 2023.

564 Chang, J. and Hanna, S.: Air quality model performance evaluation, *Meteorol Atmos Phys.*, 87, 167–196,
565 <https://doi.org/10.1007/s00703-003-0070-7>, 2004.

566 Chuang, M. T, Fu, J. S., Lee, C., Lin, N., Gao, Y., Wang, S., Sheu, G., Hsiao, T., Wang, J., Yen, M., Lin,
567 T., and Thongboonchoo, N.: The Simulation of Long-Range Transport of Biomass Burning Plume and
568 Short-Range Transport of Anthropogenic Pollutants to a Mountain Observatory in East Asia during the
569 7-SEAS / 2010 Dongsha Experiment, 2933–2949, <https://doi.org/10.4209/aaqr.2015.07.0440>, 2016.

570 Chuang, M. T., Fu, J. S., Jang, C. J., Chan, C. C., Ni, P. C., and Lee, C. Te: Simulation of long-range
571 transport aerosols from the Asian Continent to Taiwan by a Southward Asian high-pressure system, *Sci.*
572 *Total Environ.*, 406, 168–179, <https://doi.org/10.1016/j.scitotenv.2008.07.003>, 2008.

573 Chuang, M.-T., Ooi, M. C. G., Lin, N.-H., Fu, J. S., Lee, C.-T., Wang, S.-H., Yen, M.-C., Kong, S. S.-K.,
574 and Huang, W.-S.: Study on the impact of three Asian industrial regions on PM_{2.5} in Taiwan and the
575 process analysis during transport, *Atmos. Chem. Phys.*, 20, 14947–14967, [https://doi.org/10.5194/acp-](https://doi.org/10.5194/acp-20-14947-2020)
576 20-14947-2020, 2020.

577 Dong, X., Fu, J. S., Huang, K., Tong, D., and Zhuang, G.: Model development of dust emission and
578 heterogeneous chemistry within the Community Multiscale Air Quality modeling system and its
579 application over East Asia, *Atmos. Chem. Phys.*, 16, 8157–8180, [https://doi.org/10.5194/acp-16-8157-](https://doi.org/10.5194/acp-16-8157-2016)
580 2016, 2016.

581 Dong, X., Fu, J. S., Huang, K., Lin, N., Wang, S., and Yang, C.: Analysis of the Co-existence of Long-
582 range Transport Biomass Burning and Dust in the Subtropical West Pacific Region, *Sci. Rep.*, 1–10,
583 <https://doi.org/10.1038/s41598-018-27129-2>, 2018.

584 Dong, X., Fu, J. S., Huang, K., Zhu, Q., and Tipton, M.: Regional climate effects of biomass burning and
585 dust in East Asia: Evidence from modeling and observation, *Geophysical Research Letters*, 46,
586 <https://doi.org/10.1029/2019GL083894>, 2019.

587 Emerson, E. W., Hodshire, A. L., DeBolt, H. M., Bilsback, K. R., Pierce, J. R., McMeeking, G. R., and
588 Farmer, D. K.: Revisiting particle dry deposition and its role in radiative effect estimates, *Proc. Natl.*
589 *Acad. Sci. U. S. A.*, 117, 26076–26082, <https://doi.org/10.1073/pnas.2014761117>, 2020.

590 Foroutan, H., Young, J., Napelenok, S., Ran, L., Appel, K., Gilliam, R., and Pleim, J.: Journal of Advances
591 in Modeling Earth Systems, *J. Adv. Model. Earth Syst.*, 9, 585–606,
592 <https://doi.org/10.1002/2013MS000282>.Received, 2017.

593 Gaydos, T. M., Pinder, R., Koo, B., Fahey, K. M., Yarwood, G., and Pandis, S. N.: Development and
594 application of a three-dimensional aerosol chemical transport model, *PMCAMx, Atmos. Environ.*, 41,
595 2594–2611, <https://doi.org/10.1016/j.atmosenv.2006.11.034>, 2007.

596 Gelaro, R., McCarty, W., Suárez, M. J., Todling, R., Molod, A., Takacs, L., Randles, C. A., Darmenov,
597 A., Bosilovich, M. G., Reichle, R., Wargan, K., Coy, L., Cullather, R., Draper, C., Akella, S., Buchard,
598 V., Conaty, A., da Silva, A. M., Gu, W., Kim, G. K., Koster, R., Lucchesi, R., Merkova, D., Nielsen, J.
599 E., Partyka, G., Pawson, S., Putman, W., Rienecker, M., Schubert, S. D., Sienkiewicz, M., and Zhao, B.:
600 The modern-era retrospective analysis for research and applications, version 2 (MERRA-2), *J. Clim.*, 30,
601 5419–5454, <https://doi.org/10.1175/JCLI-D-16-0758.1>, 2017.

602 Giardina, M. and Buffa, P.: A new approach for modeling dry deposition velocity of particles, *Atmos.*
603 *Environ.*, 180, 11–22, <https://doi.org/10.1016/j.atmosenv.2018.02.038>, 2018.

604 Gui, K., Yao, W., Che, H., An, L., Zheng, Y., Li, L., Zhao, H., Zhang, L., Zhong, J., Wang, Y., and Zhang,
 605 X.: Record-breaking dust loading during two mega dust storm events over northern China in March 2021:
 606 aerosol optical and radiative properties and meteorological drivers, *Atmos. Chem. Phys.*, 22, 7905–7932,
 607 <https://doi.org/10.5194/acp-22-7905-2022>, 2022.

608 Han, X., Ge, C., Tao, J., Zhang, M., and Zhang, R.: Air quality modeling for a strong dust event in East
 609 Asia in March 2010, *Aerosol Air Qual. Res.*, 12, 615–628, <https://doi.org/10.4209/aaqr.2011.11.0191>,
 610 2012.

611 He, Y., Yi, F., Yin, Z., Liu, F., Yi, Y., and Zhou, J.: Mega Asian dust event over China on 27–31 March
 612 2021 observed with space-borne instruments and ground-based polarization lidar, *Atmos. Environ.*, 285,
 613 119238, <https://doi.org/10.1016/j.atmosenv.2022.119238>, 2022.

614 Hogrefe, C., Bash, J. O., Pleim, J. E., Schwede, D. B., Gilliam, R. C., Foley, K. M., Appel, K. W., and
 615 Mathur, R.: An analysis of CMAQ gas-phase dry deposition over North America through grid-scale and
 616 land-use-specific diagnostics in the context of AQMEII4, *Atmos. Chem. Phys.*, 23, 8119–8147,
 617 <https://doi.org/10.5194/acp-23-8119-2023>, 2023.

618 Huang, H.-Y., Wang, S.-H., Huang, W.-X., Lin, N.-H., Chuang, M.-T., da Silva, A. M., Peng, C.-M.:
 619 Influence of synoptic-dynamic meteorology on the long-range transport of Indochina biomass burning
 620 aerosols, *J. Geophys. Res.*, 111, 125, e2019JD031260. <https://doi.org/10.1029/2019JD031260>, 2020.

621 Huang, K., Fu, J. S., Lin, N.-H., Wang, S.-H., Dong, X., Wang, G.: Superposition of Gobi Dust and
 622 Southeast Asian Biomass Burning: The Effect of Multisource Long - Range Transport on Aerosol Optical
 623 Properties and Regional Meteorology Modification, *J. Geophys. Res.*, 124, 16, 9464-9483,
 624 <https://doi.org/10.1029/2018JD030241>, 2019.

625 Huang, W. S., Griffith, S. M., Lin, Y. C., Chen, Y. C., Lee, C. Te, Chou, C. C. K., Chuang, M. T., Wang,
 626 S. H., and Lin, N. H.: Satellite-based emission inventory adjustments improve simulations of long-range
 627 transport events, *Aerosol Air Qual. Res.*, 21, 1–16, <https://doi.org/10.4209/AAQR.210121>, 2021.

628 Jin, J., Pang, M., Segers, A., Han, W., Fang, L., Li, B., Feng, H., Lin, H. X., and Liao, H.: Inverse
 629 modeling of the 2021 spring super dust storms in East Asia, *Atmos. Chem. Phys.*, 22, 6393–6410,
 630 <https://doi.org/10.5194/acp-22-6393-2022>, 2022.

631 Khan, T. R. and Perlinger, J. A.: Evaluation of five dry particle deposition parameterizations for
632 incorporation into atmospheric transport models, *Geosci. Model Dev.*, 10, 3861–3888,
633 <https://doi.org/10.5194/gmd-10-3861-2017>, 2017.

634 Kok, J. F., Parteli, E. J. R., Michaels, T. I., Karam, D. B., and Pierre, U.: The physics of wind-blown sand
635 and dust, 1–119, n.d.

636 Kong, S. S.-K., Pani, S. K., Griffith, S. M., Ou-Yang, C.-F., Babu, S. R., Chuang, M.-T., Ooi, M. C. G.,
637 Huang, W.-S., Sheu, G.-R., and Lin, N.-H.: Distinct transport mechanisms of East Asian dust and the
638 impact on downwind marine and atmospheric environments, *Sci. Total Environ.*, 827, 154255,
639 <https://doi.org/10.1016/j.scitotenv.2022.154255>, 2022.

640 Kong, S. S., Fu, J. S., Dong, X., Chuang, M., Chel, M., Ooi, G., Huang, W., Griffith, S. M., Kumar, S.,
641 and Lin, N.: Sensitivity analysis of the dust emission treatment in CMAQv5. 2. 1 and its application to
642 long-range transport over East Asia, *Atmos. Environ.*, 118441,
643 <https://doi.org/10.1016/j.atmosenv.2021.118441>, 2021.

644 Kong, S. S. K., Ravindra Babu, S., Wang, S. H., Griffith, S. M., Chang, J. H. W., Chuang, M. T., Sheu,
645 G. R., and Lin, N. H.: Expanding the simulation of East Asian super dust storms: physical transport
646 mechanisms impacting the western Pacific, *Atmos. Chem. Phys.*, 24, 1041–1058,
647 <https://doi.org/10.5194/acp-24-1041-2024>, 2024.

648 Li, M., Zhang, Q., Kurokawa, J.-I., Woo, J.-H., He, K., Lu, Z., Ohara, T., Song, Y., Streets, D. G.,
649 Carmichael, G. R., Cheng, Y., Hong, C., Huo, H., Jiang, X., Kang, S., Liu, F., Su, H., and Zheng, B.:
650 MIX: a mosaic Asian anthropogenic emission inventory under the international collaboration framework
651 of the MICS-Asia and HTAP, *Atmos. Chem. Phys.*, 17, 935–963, [https://doi.org/10.5194/acp-17-935-](https://doi.org/10.5194/acp-17-935-2017)
652 2017, 2017.

653 Liang, L., Han, Z., Li, J., Xia, X., Sun, Y., Liao, H., Liu, R., and Liang, M.: Science of the Total
654 Environment Emission, transport, deposition, chemical and radiative impacts of mineral dust during
655 severe dust storm periods in March 2021 over East Asia, *Sci. Total Environ.*, 852, 158459,
656 <https://doi.org/10.1016/j.scitotenv.2022.158459>, 2022.

657 Liu, S., Xing, J., Sahu, S. K., Liu, X., Liu, S., Jiang, Y., Zhang, H., Li, S., Ding, D., Chang, X., and Wang,
 658 S.: Wind-blown dust and its impacts on particulate matter pollution in Northern China: Current and future
 659 scenarios, *Environ. Res. Lett.*, 16, 114041, <https://doi.org/10.1088/1748-9326/ac31ec>, 2021.

660 Massad, R. S., Nemitz, E., and Sutton, M. A.: Review and parameterisation of bi-directional ammonia
 661 exchange between vegetation and the atmosphere, *Atmos. Chem. Phys.*, 10, 10359–10386,
 662 <https://doi.org/10.5194/acp-10-10359-2010>, 2010.

663 Nemitz, E., Milford, C., and Sutton, M. A.: A two-layer canopy compensation point model for describing
 664 bi-directional biosphere-atmosphere exchange of ammonia, *Q. J. R. Meteorol. Soc.*, 127, 815–833,
 665 <https://doi.org/10.1256/smsqj.57305>, 2001.

666 Ooi, M., Chuang, M.-T., Fu, J., Kong, S., Huang, W.-S., Wang, S.-H., Chan, A., Pani, S., and Lin, N.-H.:
 667 Improving prediction of trans-boundary biomass burning plume dispersion: from northern peninsular
 668 Southeast Asia to downwind western north Pacific Ocean, *Atmos. Chem. Phys.*, 20, 14947–14967,
 669 <https://doi.org/10.5194/acp-2020-1283>, 2021.

670 Pani, S. K., Wang, S. H., Lin, N. H., Lee, C. Te, Tsay, S. C., Holben, B. N., Janjai, S., Hsiao, T. C.,
 671 Chuang, M. T., and Chantara, S.: Radiative effect of springtime biomass-burning aerosols over northern
 672 indochina during 7-SEAS/BASELInE 2013 campaign, *Aerosol Air Qual. Res.*, 16, 2802–2817,
 673 <https://doi.org/10.4209/aaqr.2016.03.0130>, 2016.

674 Pani, S. K., Wang, S. H., Lin, N. H., Chantara, S., Lee, C. Te, and Thepnuan, D.: Black carbon over an
 675 urban atmosphere in northern peninsular Southeast Asia: Characteristics, source apportionment, and
 676 associated health risks, *Environ. Pollut.*, 259, 113871, <https://doi.org/10.1016/j.envpol.2019.113871>,
 677 2020.

678 Pleim, J. E., Ran, L., Saylor, R. D., Willison, J., and Binkowski, F. S.: A New Aerosol Dry Deposition
 679 Model for Air Quality and Climate Modeling, *J. Adv. Model. Earth Syst.*, 14, 1–21,
 680 <https://doi.org/10.1029/2022MS003050>, 2022.

681 Ramanathan, V and Carmicheal, G.: Climate change due to BC, *Nat. Geosci.*, 1, 221–227, 2008.

682 Ravindra Babu, S., Ou-Yang, C. F., Griffith, S. M., Pani, S. K., Kong, S. S. K., and Lin, N. H.: Transport
 683 pathways of carbon monoxide from Indonesian fire pollution to a subtropical high-Altitude mountain site

684 in the western North Pacific, *Atmos. Chem. Phys.*, 23, 4727–4740, [https://doi.org/10.5194/acp-23-4727-](https://doi.org/10.5194/acp-23-4727-2023)
685 2023, 2023.

686 Ryu, Y. H. and Min, S. K.: Improving Wet and Dry Deposition of Aerosols in WRF-Chem: Updates to
687 Below-Cloud Scavenging and Coarse-Particle Dry Deposition, *J. Adv. Model. Earth Syst.*, 14,
688 <https://doi.org/10.1029/2021MS002792>, 2022.

689 Saylor, R. D., Baker, B. D., Lee, P., Tong, D., Pan, L., and Hicks, B. B.: The particle dry deposition
690 component of total deposition from air quality models: right, wrong or uncertain?, *Tellus, Ser. B Chem.*
691 *Phys. Meteorol.*, 71, 1–22, <https://doi.org/10.1080/16000889.2018.1550324>, 2019.

692 Shu, Q., Koo, B., Yarwood, G., and Henderson, B. H.: Strong influence of deposition and vertical mixing
693 on secondary organic aerosol concentrations in CMAQ and CAMx, *Atmos. Environ.*, 171, 317–329,
694 <https://doi.org/10.1016/j.atmosenv.2017.10.035>, 2017.

695 Shu, Q., Murphy, B., Schwede, D., Henderson, B. H., Pye, H. O. T., Appel, K. W., Khan, T. R., and 534
696 Perlinger, J. A.: Improving the particle dry deposition scheme in the CMAQ photochemical modeling 535
697 system, *Atmos. Environ.*, 289, 119343, <https://doi.org/10.1016/j.atmosenv.2022.119343>, 2022.

698 Slinn, W. G. N.: Predictions for particle deposition to vegetative canopies, *Atmos. Environ.*, 16, 1785–
699 1794, [https://doi.org/10.1016/0004-6981\(82\)90271-2](https://doi.org/10.1016/0004-6981(82)90271-2), 1982.

700 Tang, W., Dai, T., Cheng, Y., Wang, S., and Liu, Y.: A Study of a Severe Spring Dust Event in 2021 over
701 East Asia with WRF-Chem and Multiple Platforms of Observations, *Remote Sens.*, 14, 3795,
702 <https://doi.org/10.3390/rs14153795>, 2022.

703 Tav, J., Masson, O., Burnet, F., Paulat, P., Bourrienne, T., Conil, S. and Pourcelot, L.: Determination of
704 Fog-Droplet Deposition Velocity from a Simple Weighing Method. *Aerosol Air Qual. Res.* 18: 103-113.
705 <https://doi.org/10.4209/aaqr.2016.11.0519>, 2018.

706 Wang, W., Zhou, H., Lyu, R., Shao, L., Li, W., Xing, J., Zhao, Z., Li, X., Zhou, X., and Zhang, D.:
707 Organic Carbon and Elemental Carbon in Two Dust Plumes at a Coastal City in North China, *Aerosol*
708 *Air Qual. Res.*, 24, <https://doi.org/10.4209/aaqr.240002>, 2024.

709 Wesley, M. L.: Parameterization of Surface Resistances to Gaseous Dry Deposition in Regional-Scale
710 Numerical Models, *Atmos. Environ.*, 23, 1293–1304, 1989.

711 Xiao, H. W., Xu, Y., and Xiao, H. Y.: Source apportionment of black carbon aerosols in winter across
 712 China, *Atmos. Environ.*, 298, <https://doi.org/10.1016/j.atmosenv.2023.119622>, 2023.
 713 Zeng, Y., Wang, M., Zhao, C., Chen, S., Liu, Z., Huang, X., and Gao, Y.: WRF-Chem v3.9 simulations
 714 of the East Asian dust storm in May 2017: Modeling sensitivities to dust emission and dry deposition
 715 schemes, *Geosci. Model Dev.*, 13, 2125–2147, <https://doi.org/10.5194/gmd-13-2125-2020>, 2020.
 716 Zhang, L., Gong, S., Padro, J., and Barrie, L.: A size-segregated particle dry deposition scheme for an
 717 atmospheric aerosol module, *Atmos. Environ.*, 35, 549–560, [https://doi.org/10.1016/S1352-](https://doi.org/10.1016/S1352-2310(00)00326-5)
 718 2310(00)00326-5, 2001.
 719 Zhang, L., Zhang, H., Li, Q., Cai, X., and Song, Y.: Vertical dispersion mechanism of long-range
 720 transported dust in Beijing: Effects of atmospheric turbulence, *Atmos. Res.*, 269, 106033,
 721 <https://doi.org/10.1016/j.atmosres.2022.106033>, 2022.
 722 Zhang, X.-X., Sharratt, B., Chen, X., Wang, Z.-F., Liu, L.-Y., Guo, Y.-H., Li, J., Chen, H.-S., and Yang,
 723 W.-Y.: Dust deposition and ambient PM10 concentration in northwest China: spatial and temporal
 724 variability, *Atmos. Chem. Phys.*, 17, 1699–1711, <https://doi.org/10.5194/acp-17-1699-2017>, 2017.
 725 Zheng, B., Tong, D., Li, M., Liu, F., Hong, C., Geng, G., Li, H., Li, X., Peng, L., Qi, J., Yan, L., Zhang,
 726 Y., Zhao, H., Zheng, Y., He, K., and Zhang, Q.: Trends in China's anthropogenic emissions since 2010
 727 as the consequence of clean air actions, *Atmos. Chem. Phys.*, 18, 14095–14111,
 728 <https://doi.org/10.5194/acp-18-14095-2018>, 2018.

729

730

731

732

733

734

735

736

737

738

739

740

741

742

743 **Table 1.** Detailed mechanism expression relating the three dry deposition schemes.

Schemes	Surfaces	S22 (CMAQv5.3 and beyond)	E20	P22
V_d		$f_{veg} V_d \text{ vegetated} + (1-f_{veg}) V_d \text{ smooth}$	$f_{veg} V_d \text{ vegetated} + (1-f_{veg}) V_d \text{ smooth}$	$f_{veg} V_d \text{ vegetated} + (1-f_{veg}) V_d \text{ smooth}$
R_b	Vegetated	$\frac{1}{f_{veg}((\max(LAI, 1.0))u_*(E_B + E_{Im}))}$	$\frac{1}{\text{wet} * E_{Tot \text{ veg}} + (1 - \text{wet}) * E_{Tot \text{ veg}} * R1}$	$\frac{1}{f_{veg}((\max(LAI, 1.0))u_*(E_B + E_{Im}))}$
R_b	Smooth	$\frac{1}{u_*(E_B + E_{Im})}$	$\frac{1}{\text{wet} * E_{Tot \text{ smth}} + (1 - \text{wet}) * E_{Tot \text{ smth}} * R1}$	$\frac{1}{BAI \cdot u_*(E_B + E_{Im})}$
E_B	Vegetated	$Sc^{-2/3}$	$C_B Sc^{-2/3}$	$C_{IB} Sc^{-2/3}$
E_B	Smooth	$Sc^{-2/3}$	$C_B Sc^{-2/3}$	$f_{wc} \frac{u_*}{U_{10}} + (1-f_{wc}) C_{IB} Sc^{-2/3}$
E_{Im}	Vegetated	$\frac{St^2}{St^2 + 1}$	$C_{Im} (\frac{St}{St+\alpha})^{1.7}$	$f_{micro} \frac{St h^2}{St h^2 + 1} + (1-f_{micro}) \frac{St 1^2}{St 1^2 + 1}$
E_{Im}	Smooth	$\frac{St^2}{St^2 + 400}$	$C_{Im} (\frac{St}{St+100})^{1.7}$	$10^{-3/St}$
E_{In}	Vegetated	0	$C_{In} (\frac{d_p}{A})^{0.8}$	0
E_{In}	Smooth	0	0	0

744 $V_d \text{ vegetated}$ = deposition velocity over the vegetative surface: $V_d \text{ vegetated} = \frac{V_g}{1 - \exp(-V_g(R_a + R_b \text{ vegetated}))}$

745 $V_d \text{ smooth}$ = deposition velocity over the smooth surface: $V_d \text{ smooth} = \frac{V_g}{1 - \exp(-V_g(R_a + R_b \text{ smooth}))}$

746 f_{veg} = grid scale vegetation-coverage fraction

747 E_B = Brownian diffusion efficiency

748 E_{Im} = Impaction efficiency

749 E_{In} = Interception efficiency

750 Sc = Schmidt number

751 St = Stokes number

752 wet = Wet surface

753 $E_{Tot \text{ veg}}$ = $\text{veg_ustar} * (E_B + E_{Im} + E_{In})$

754 $E_{Tot \text{ smth}}$ = $3.0 * \text{ustg} * (E_B + E_{Im})$

755 $R1$ = Bounce correction term by Slinn (1982).

756 C_B = Brownian collective coefficient: 0.2

757 C_{Im} = Impaction collective coefficient: 0.4

758 C_{In} = Interception collective coefficient: 2.5

759 α = Empirical constant

760 LAI = Leaf area index

761 BAI = Building area index

762 C_{IB} = 1.0/3.0

763 f_{wc} = Whitecap surface fraction

764 f_{micro} = Total impaction fraction from the microscale features

765 u_* and U_{10} = Frictional velocity and wind speed at 10 m (ms^{-1})

766 $St1$ and $St h$ = Obstacle characteristic dimensions for the leaf hairs and microscale roughness on leaves

767 **Table 2.** Model settings.

Model setting	Descriptions
Period	12 March-20 April 2021 and 22-31 January 2023
Domain	d01, d02, and d03 with 45 KM, 15 KM, and 5 KM of the resolutions, respectively
Boundary condition	NCEP FNL lateral boundary condition
Surface and land surface model	NOAH
Numerical weather model	WRF v40, including grid and observation nudging at d01.
Chemical transport model	CMAQ v5.4
Gas-phase chemistry and aerosol mechanism	CB06e51 + AE7
Emission Inventory	MICS-ASIA III emission in 2023, adjusted from the emission in 2017 (Zhang et al., 2018) based on the OMI-NO _x satellite (Huang et al., 2021).
Online dust treatment	The refined windblown dust treatment suggested by Kong et al. (2024).
Dry deposition option	STAGE (S22, E20 and P22).

768
769
770
771
772
773
774
775
776
777
778
779
780
781
782
783
784
785
786
787
788
789
790
791
792

793 **Table 3.** Simulation scenarios used in this present study.

Experiments	Online dust emission treatment by Kong et al. (2024)	Dry deposition treatment	Surface resistance (R_b) at the smooth surface
CMAQ_Off_S22	Off	S22	Default
CMAQ_Dust_S22	On	S22	Default
CMAQ_Dust_E20	On	E20	Default
CMAQ_Dust_P22	On	P22	Default
CMAQ_Dust_P22E01	On	P22	Increased by a factor of 10
CMAQ_Dust_P22E02	On	P22	Increased by a factor of 50
CMAQ_Dust_P22E03	On	P22	Increased by a factor of 100

794
795 **Table 4.** Statistical evaluation for PM₁₀ and PM_{2.5} concentrations during 22-31 January 2023 for Cape
796 Fuguei under the multiple simulation scenarios.

Benchmark		CMAQ						
		Off_ S22	Dust_ S22	Dust_ E20	Dust_ P22	Dust_ P22E01	Dust_ P22E02	Dust_ P22E03
PM ₁₀								
MeanObs		49.97	49.97	49.97	49.97	49.97	49.97	49.97
MeanMod		23.58	26.48	29.04	23.04	25.99	27.36	27.69
NMSE		0.66	0.56	0.49	0.71	0.57	0.53	0.52
NMB	± 85%	-52.81	-47.01	-41.90	-53.90	-47.99	-45.24	-44.58
R	> 0.35	0.43	0.46	0.52	0.42	0.48	0.51	0.52
NMBF		-1.12	-0.89	-0.72	-1.17	-0.92	-0.83	-0.80
PM _{2.5}								
MeanObs		15.52	15.52	15.52	15.52	15.52	15.52	15.52
MeanMod		13.56	14.15	13.86	13.16	13.26	13.22	13.20
NMSE		0.30	0.30	0.29	0.31	0.30	0.30	0.30
NMB	± 85%	-12.63	-8.84	-10.65	-15.22	-14.54	-14.80	-14.92
R	> 0.35	0.50	0.53	0.53	0.52	0.53	0.53	0.53
NMBF		-0.14	-0.20	-0.12	-0.18	-0.17	-0.17	-0.18

797 Note: the definition of the statistical formulas NMSE: Normalized Mean Square Error; NMB: Normalized
798 Mean Bias; R: Correlation Coefficient and NMBF: Normalized Mean Bias Factor

808 **Table 5.** CMAQ evaluation for PM₁₀ and PM_{2.5} against the averaged 100 observation sites across
809 mainland China (Fig. S1) and AOD against MODIS daily observation near the dust source region (above
810 30°N) with Normalized Mean Bias (NMB) under the multiple simulation scenarios (Fig. S3). Spring
811 2021, 3.15, 3.27, and 4.18 represent the evaluation period by 12 March-20 April 2021, 14-16 March 2021,
812 26-28 March 2021, and 17-19 April 2021, respectively.

Parameters	Period	CMAQ						
		Off_ S22	Dust_ S22	Dust_ E20	Dust_ P22	Dust_ P22E01	Dust_ P22E02	Dust_ P22E03
PM ₁₀	Spring 2021	-75.00	-45.97	-25.43	-59.82	-45.09	-35.42	-32.92
PM _{2.5}	Spring 2021	-55.56	-36.29	-37.50	-42.47	-41.20	-41.51	-41.66
AOD	3.15	-80.49	-46.41	-38.97	-48.45	-44.80	-41.66	-40.80
	3.27	-80.92	-41.84	-36.39	-44.52	-41.60	-39.30	-38.72
	4.18	-83.09	-7.83	-3.20	-14.52	-9.45	-7.18	-6.67
	Mean AOD	-81.50	-32.03	-26.19	-35.83	-31.95	-29.38	-28.73

813
814 **Table 6.** Average deposition velocity in January 2023 (S22_2023, E20_2023, and P22_2023) and Spring
815 2021 (S22_2021, E20_2021, and P22_2021) for Aitken, Accumulation, and Coarse modes over land and
816 ocean boundary layer, respectively.

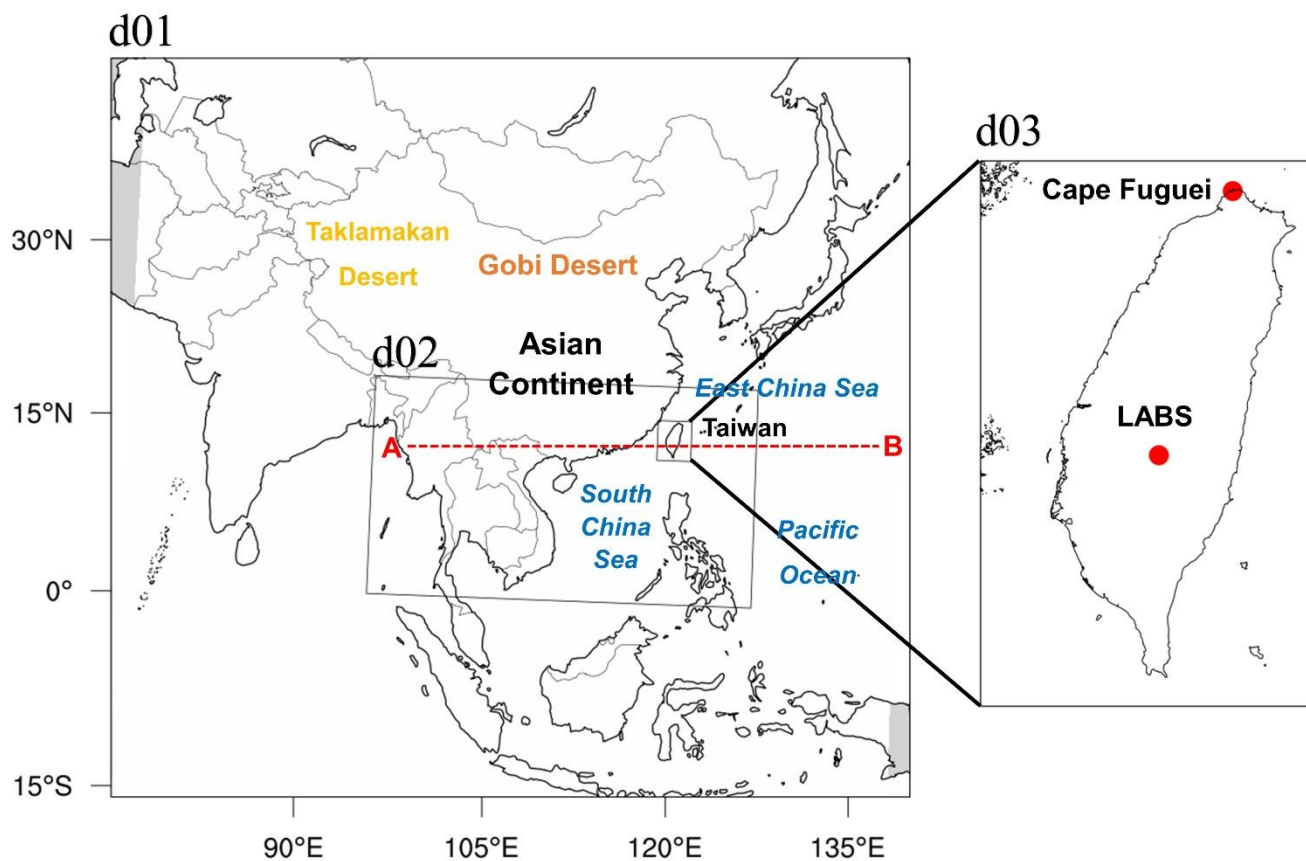
Dry deposition schemes (cm s ⁻¹)	Aitken		Accumulation		Coarse	
	Land	Ocean	Land	Ocean	Land	Ocean
S22_2023	0.219	0.117	0.120	0.064	0.078	0.085
E20_2023	0.090	0.074	0.065	0.040	0.139	0.060
P22_2023	0.085	0.062	0.072	0.043	0.290	0.116
S22_2021	0.308	0.100	0.109	0.042	0.077	0.060
E20_2021	0.139	0.063	0.063	0.026	0.142	0.053
P22_2021	0.119	0.047	0.072	0.025	0.265	0.070

817
818
819
820
821
822
823
824
825

826 **Table 7.** Model averaged dry, wet deposition and mass concentration for dust and BC aerosols in January
 827 2023 (10-days averaged) for different simulation scenarios.

Dust (ASOIL)	Dry deposition (mg m ⁻²)	Wet deposition (mg m ⁻²)	Mass concentration at the surface (µg m ⁻³)	Mass concentration at 700 hPa (µg m ⁻³)
S22	0.267	0.112	6.34	3.62
E20	0.167	0.136	10.25	4.40
P22	0.300	0.103	4.79	3.56
P22E01	0.243	0.117	7.00	3.79
P22E02	0.196	0.129	8.78	4.13
P22E03	0.183	0.132	9.28	4.22
BC (AECI + AECJ)	Dry deposition (µg m ⁻²)	Wet deposition (µg m ⁻²)	Mass concentration at the surface (ng m ⁻³)	Mass concentration at 700 hPa (ng m ⁻³)
S22	5.13	50.49	492	60.04
E20	8.09	48.27	471	57.73
P22	17.79	40.96	411	50.95
P22E01	16.88	41.64	415	51.23
P22E02	16.82	41.67	415	51.27
P22E03	16.82	41.67	415	51.27

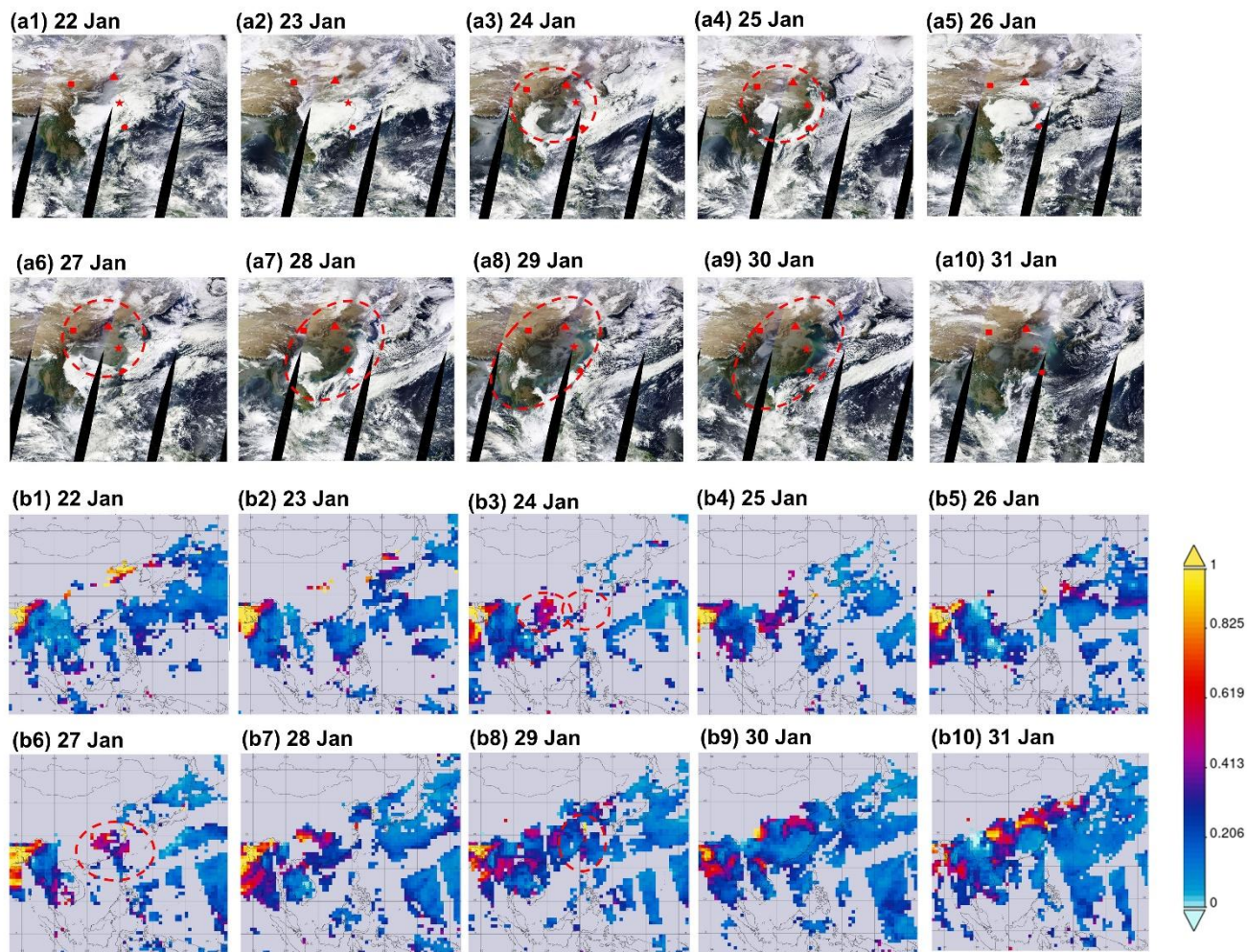
828



829

830 **Figure 1:** Modeling domain configuration in East Asia. Ground-based air quality stations in Taiwan at
 831 Cape Fuguei and Lulin Atmospheric Background Station (LABS) are shown in the zoomed panel. The
 832 red dash line (A→B) represents the transects that the aerosol plumes traveled along in this study and that
 833 are discussed in Section 3.4;

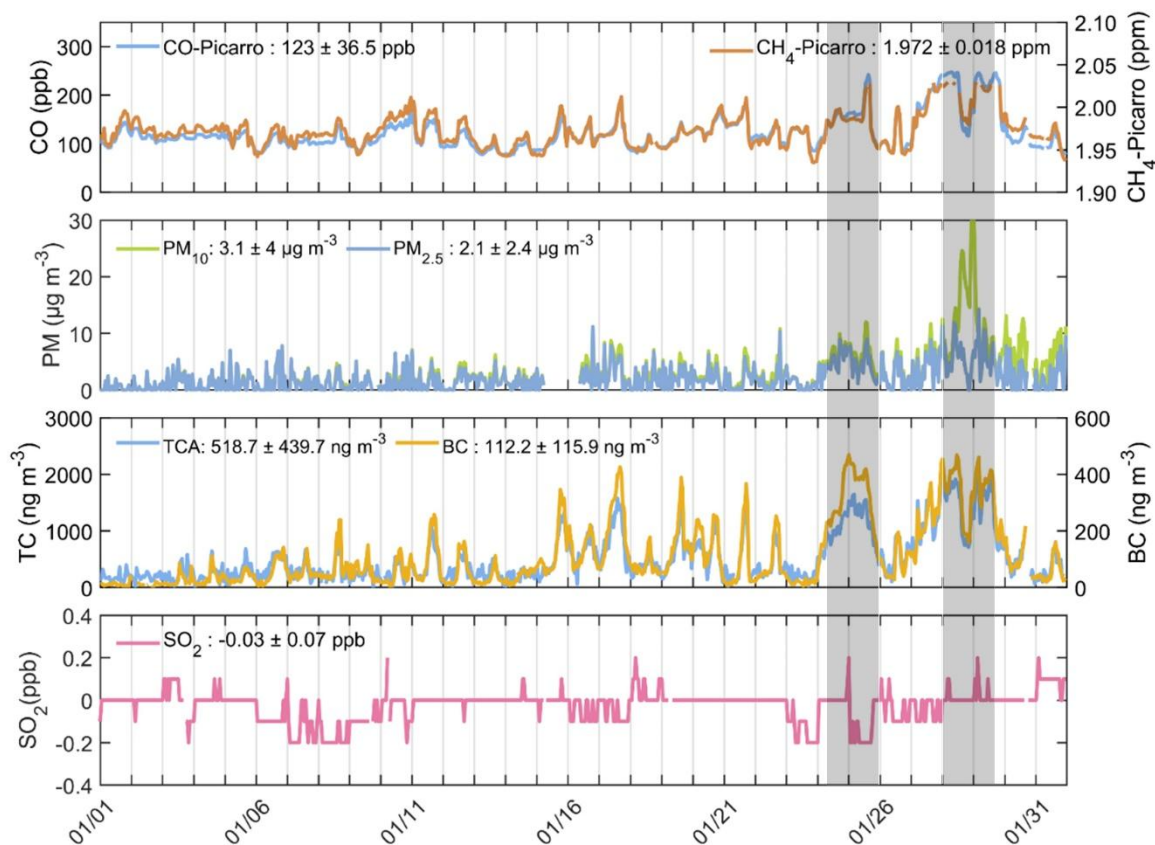
834



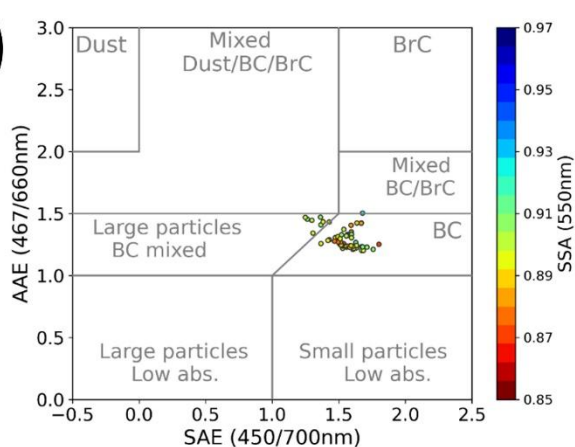
835
836 **Figure 2:** MODIS Terra images (a1-a10) and MODIS aerosol optical depth AOD at 550 nm (b1-b10)
837 showing dust outbreak across East Asia during 22-31 January 2023. Red Rectangular, triangle, star and
838 circle indicate Lanzhou, Beijing, Shanghai and Taiwan. The red circle with dash line indicates the dust
839 plume.

840

(a)



(b)



(c)

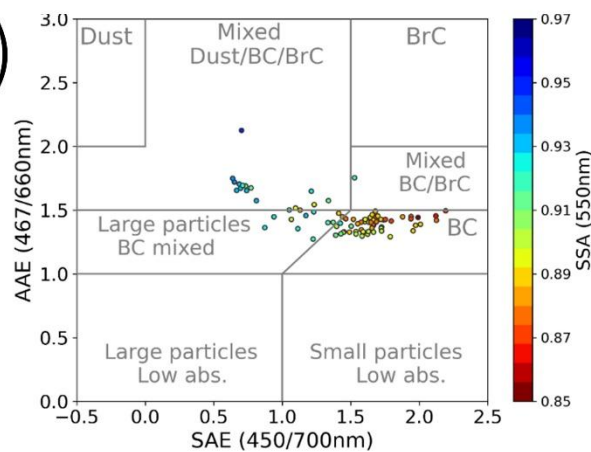


Figure 3: (a) Time series of observed pollutants over LABS during January 2023. The aerosol radiation properties during (b) 24-26 January and (c) 27-30 January 2023.

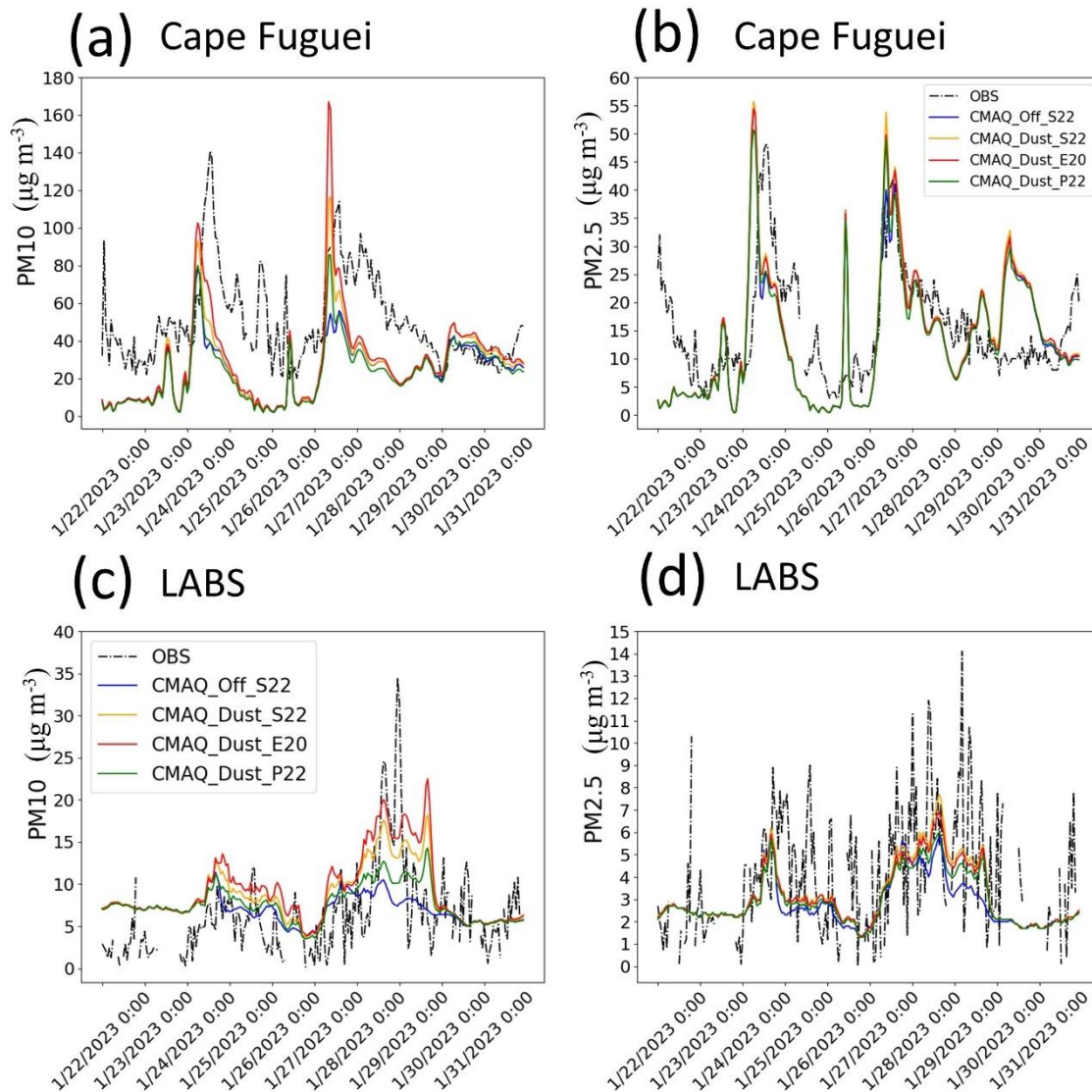
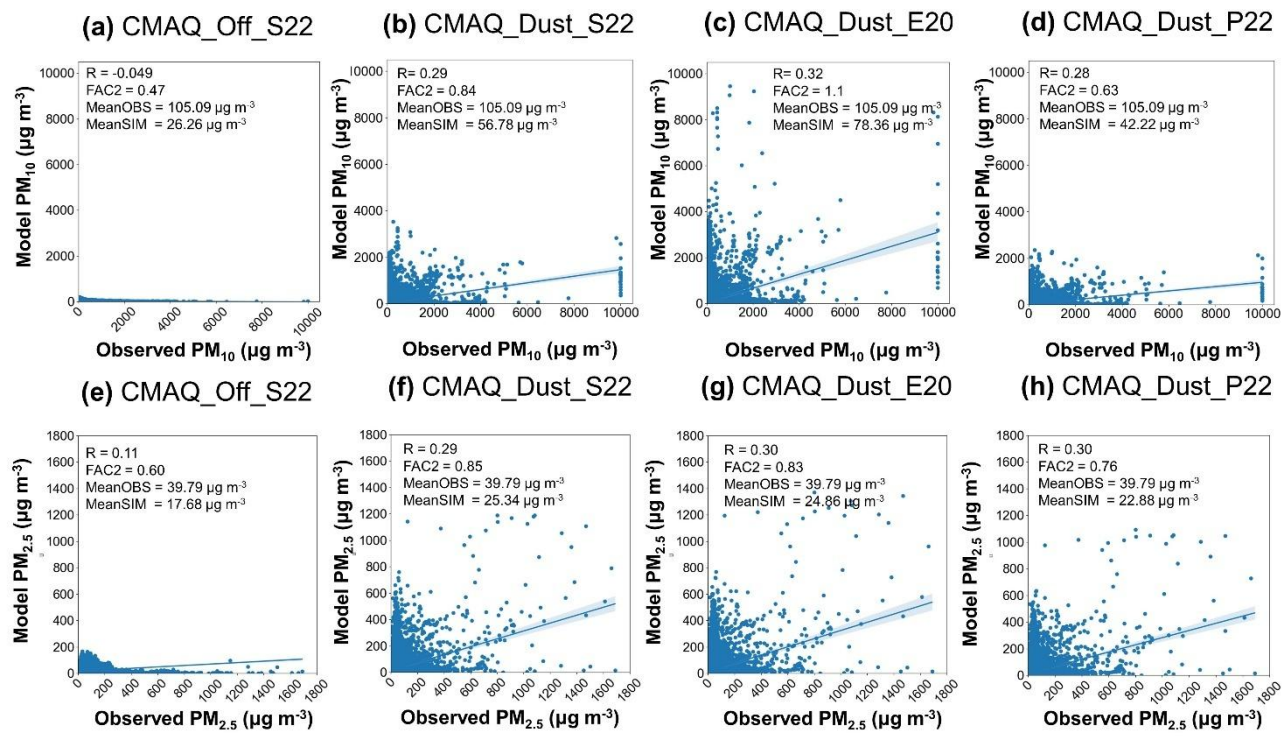


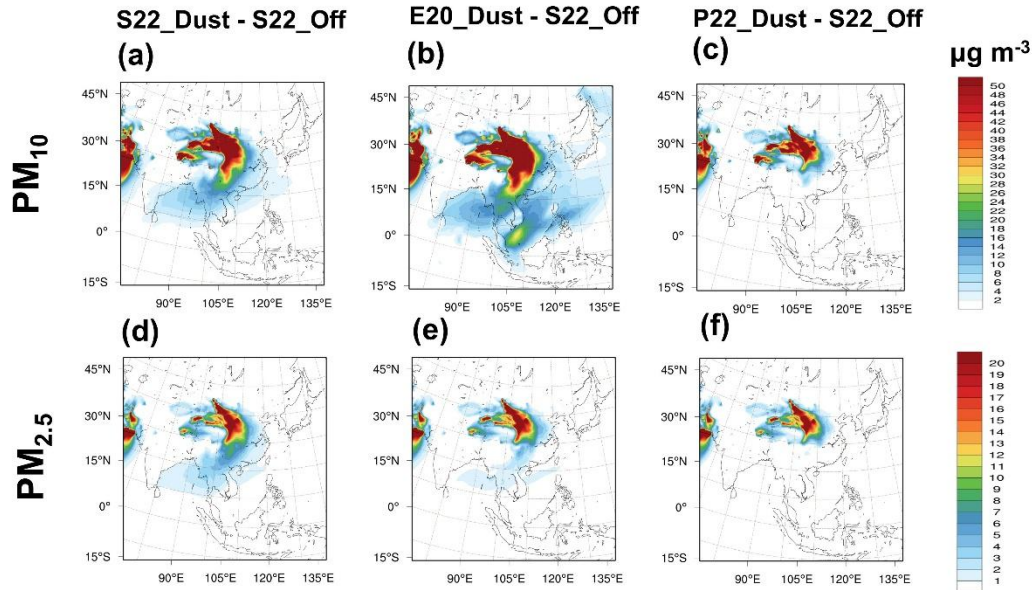
Figure 4: Time series of PM₁₀ (left panel) and PM_{2.5} (right panel) concentrations during 22-31 January 2023 under multiple deposition schemes over the Cape Fuguei (upper panel) and LABS (lower panel), representing the surface and high altitude, respectively.



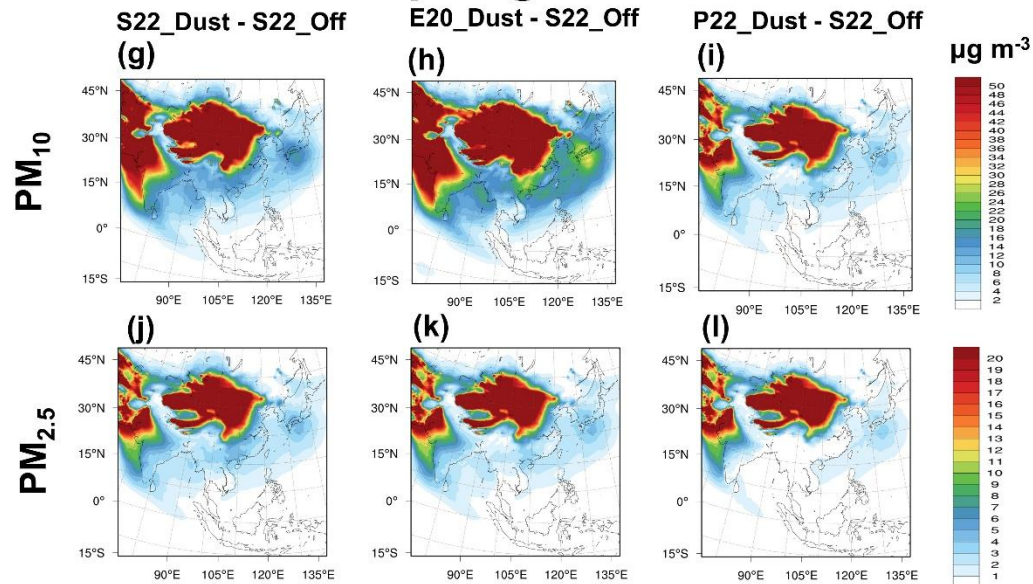
855

856 **Figure 5:** The scatter plot of the observed against modeled PM_{10} (a-d) and $PM_{2.5}$ (e-h) for
857 CMAQ_Off_S22 (a, e), CMAQ_Dust_S22 (b, f), CMAQ_Dust_E20 (c, g) and CMAQ_Dust_P22 (d, h)
858 at the 100 sites of the mainland China on 12 March-20 April 2021 (<http://>). R is the correlation coefficient
859 between the observation and model; FAC2 is the factor of two; MeanOBS and MeanSIM are the mean of
860 PM from observation and model, respectively.

January 2023



Spring 2021

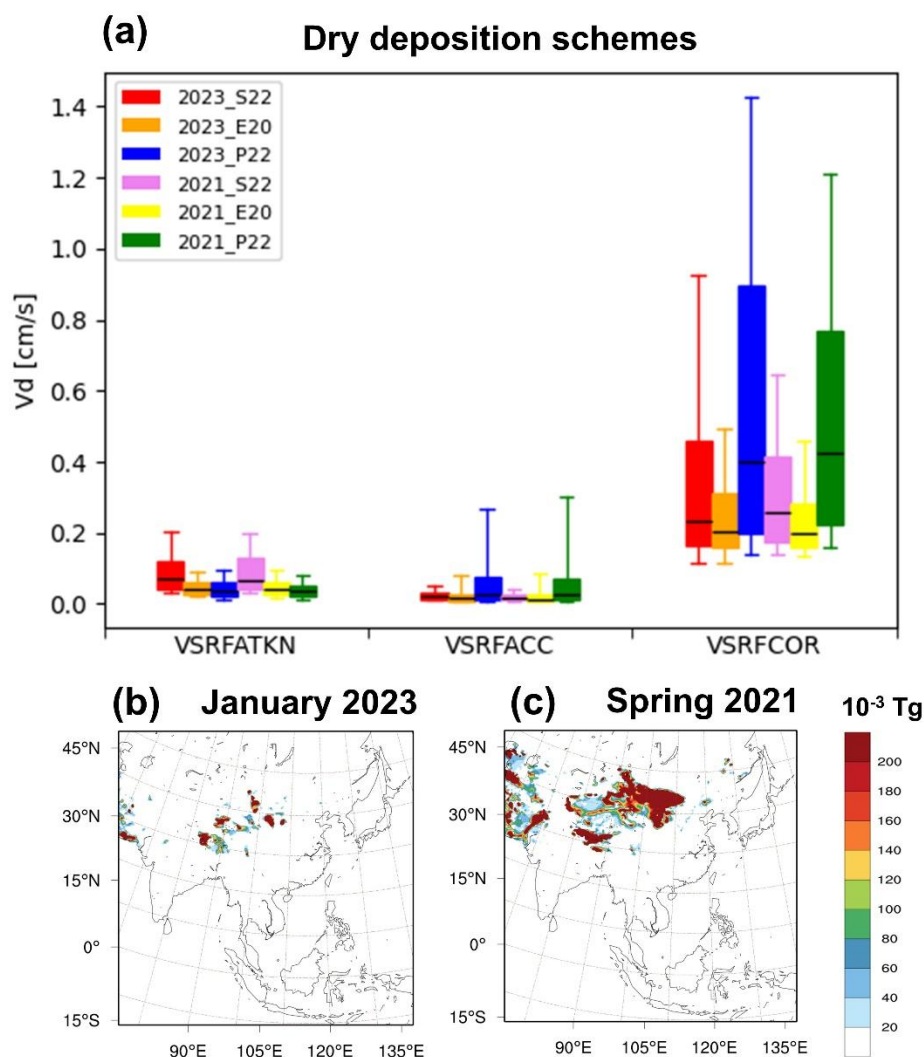


861

862 **Figure 6:** CMAQ estimated 10 days (January 2023) (a-f) and 40 days (Spring 2021) (g-l) averaged mean

863 (a, b, c, g, h, i) PM_{10} and (d, e, f, j, k, l) $PM_{2.5}$ for the concentration changes using (a, d, g, j) S22, (b, e, h,

864 k) E20 and (c, f, i, l) P22 schemes, as relative to the CMAQ_Off_S22 scenarios.

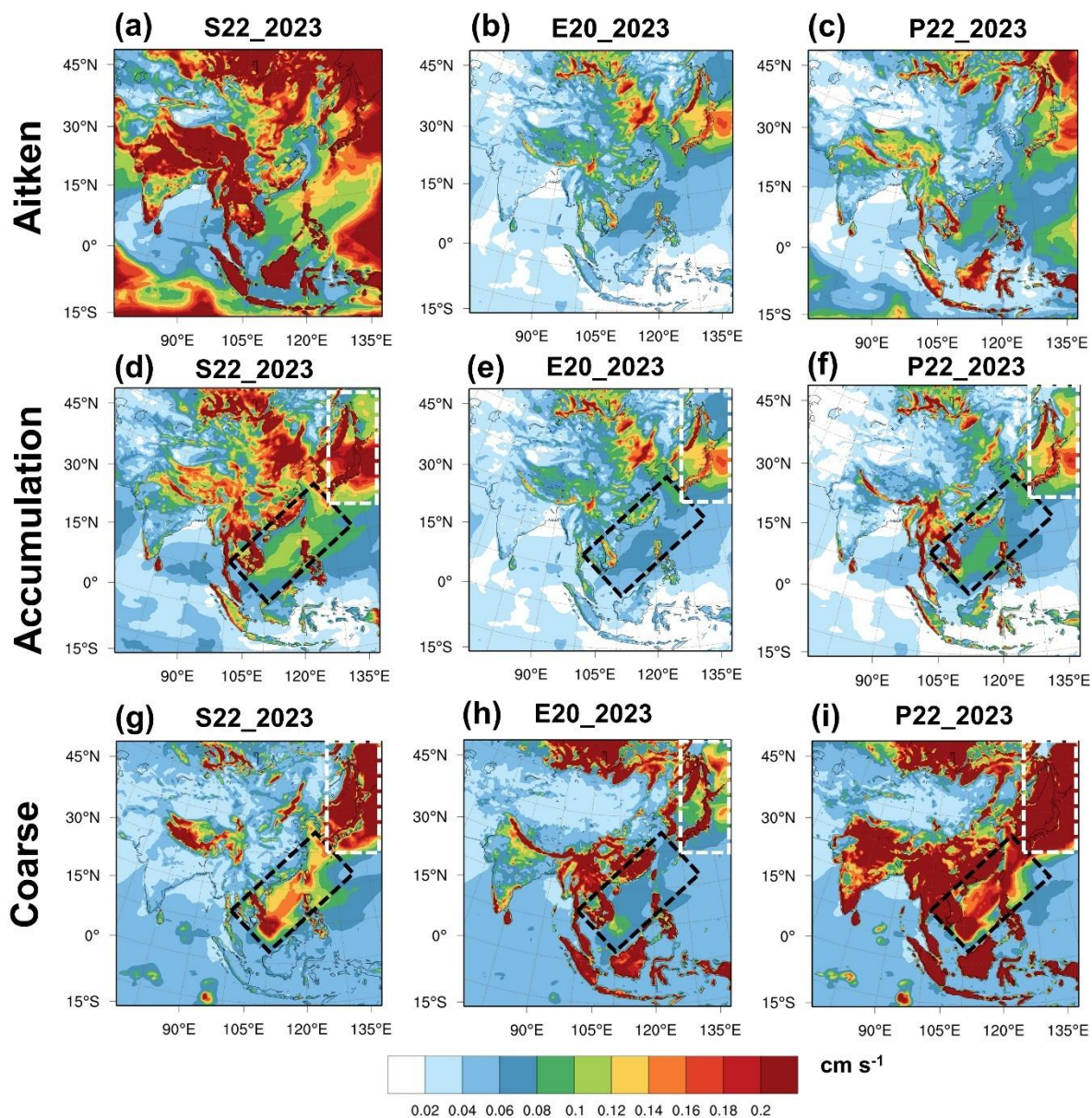


865

866 **Figure 7:** (a) 10-days (2023) and 40-days (2021) averaged dry V_d predicted by CMAQ for the Aitken,
 867 accumulation, and coarse particle modes using the 2023_S22 (red), 2023_E20 (orange), 2023_P22 (blue),
 868 2021_S22 (violet), 2021_E20 (yellow) and 2021_P22 (green) particle dry deposition schemes. The
 869 variability illustrated by the boxes and whiskers corresponds to spatial variability in annually averaged
 870 values throughout the CMAQ domain. The simulated total dust emission from CMAQ_Dust_E20 in (b)
 871 January 2023 and (c) Spring 2021.

872

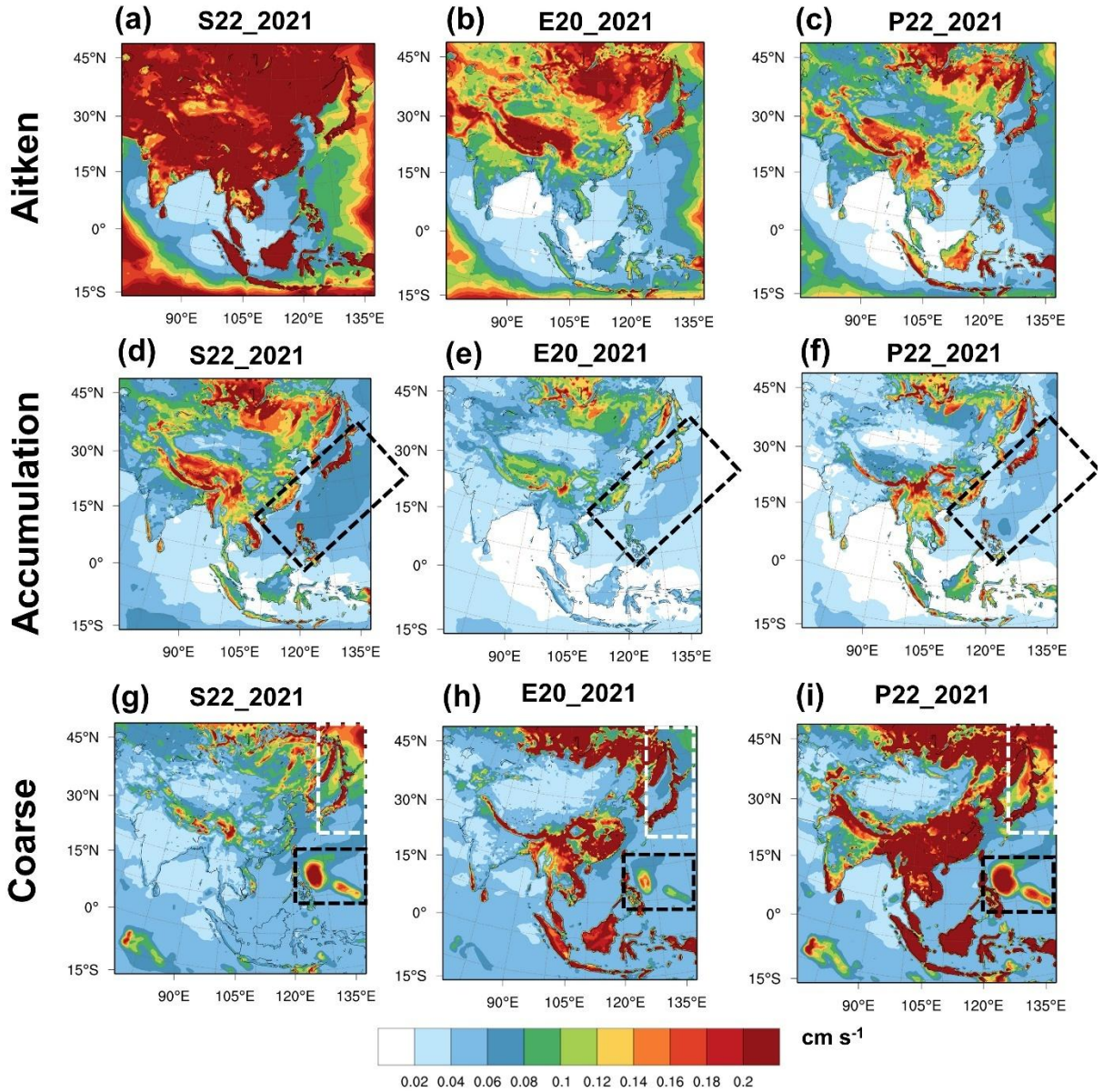
January 2023



873

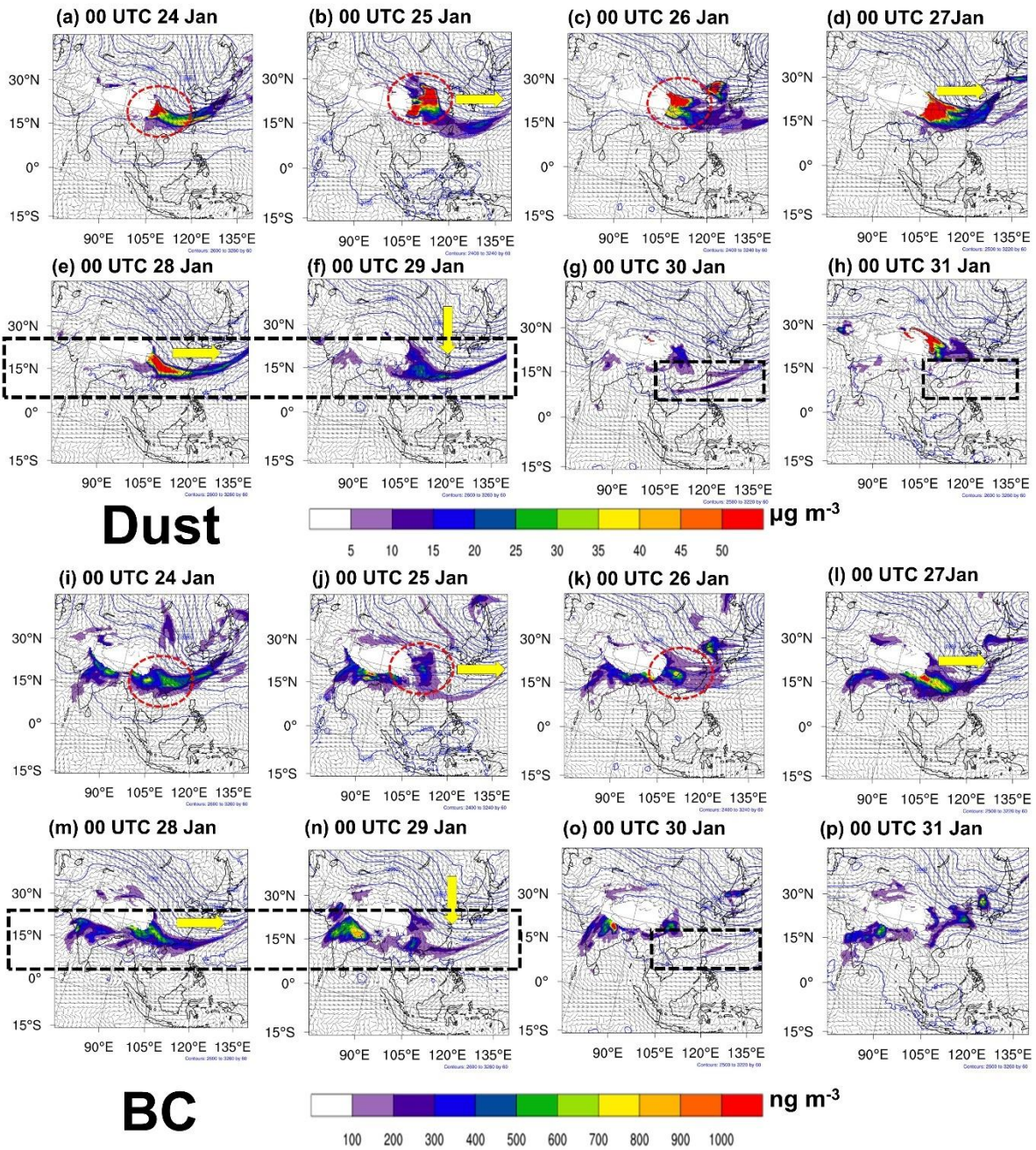
874 **Figure 8:** CMAQ estimated 10 days (22-31 January 2023) averaged for the (a-c) Aitken, (d-f)
 875 accumulation, and (g-i) coarse particle modes for (a, d, g) S22, (b, e, h) E20, and (c, f, i) P22 dry deposition
 876 schemes. White-dash rectangular indicates the region across northwest China; Black-dash rectangular
 877 indicates the marine boundary layer at the western Pacific.

Spring 2021



878

879 **Figure 9:** CMAQ estimated 40 days (12 Mar-20 April 2021) averaged for the (a-c) Aitken, (d-f)
 880 accumulation, and (g-i) coarse particle modes for (a, d, g) S22, (b, e, h) E20, and (c, f, i) P22 dry deposition
 881 schemes. White-dash rectangular indicates the region across northwest China; Black-dash rectangular
 882 indicates the marine boundary layer at the western Pacific.



883

884 **Figure 10:** CMAQ_Dust_E20 simulated mineral dust (a-h) and BC aerosol (i-p) concentrations at the
 885 700 hPa during 12 UTC 24-31 January 2023. The yellow arrows highlight the trough moving direction.
 886 The dash-black rectangular box highlights the aerosol belt.

887

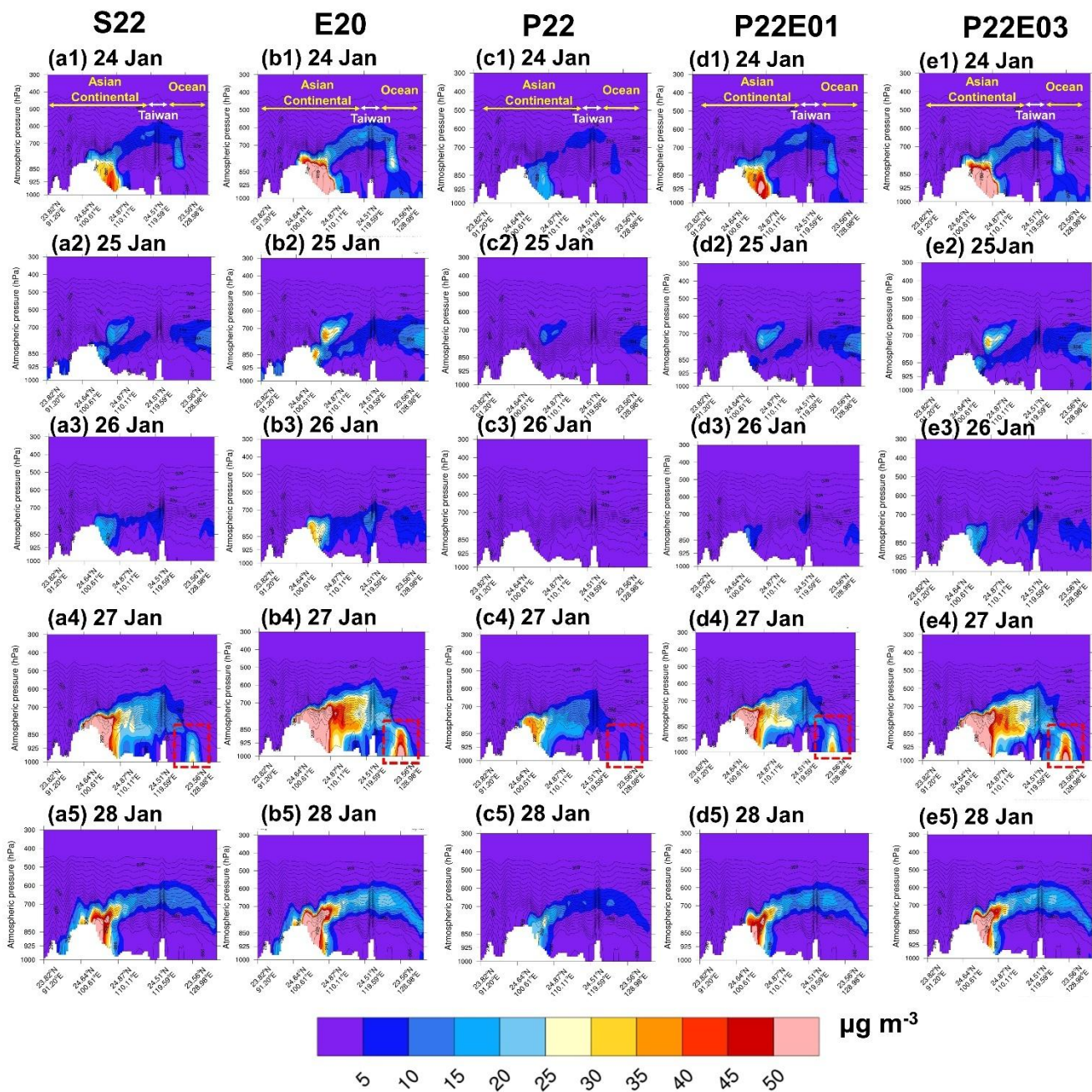
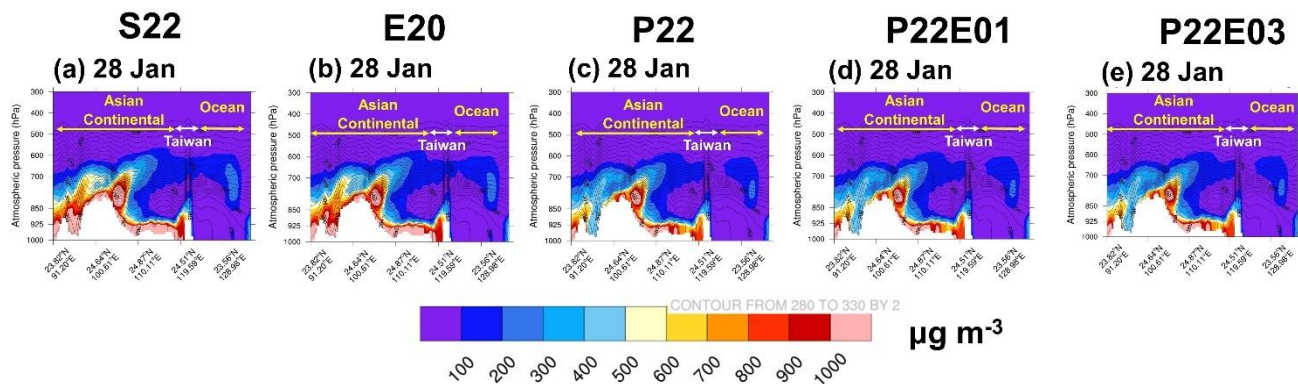


Figure 11: Vertical cross section of the simulated dust aerosol for the CMAQ_DUST (S22, E20, P22, P22E01 and P22E03) during 12 UTC 24-28 January 2023.



893

894 **Figure 12:** Vertical cross section of the simulated BC aerosol for the CMAQ_DUST (S22, E20, P22,

895 P22E01 and P22E03) during 00 UTC 28 January 2023.